

The two-loop power spectrum in redshift space

Petter Taule,^a Mathias Garny^b

^aInstitut de physique théorique, Université Paris Saclay CEA, CNRS, 91191 Gif-sur-Yvette, France

^bPhysik Department T31, Technische Universität München, James-Franck-Straße 1, D-85748 Garching, Germany

E-mail: petter.taule@ipht.fr, mathias.garny@tum.de

Abstract. We present the matter power spectrum in redshift space including two-loop corrections. We follow a strictly perturbative approach incorporating all non-linearities entering both via the redshift-space mapping and within real space up to the required (fifth) order, complemented by suitable effective field theory (EFT) corrections. This approach can a priori be viable up to scales of order $0.2h \text{ Mpc}^{-1}$ beyond which power suppression related to the finger-of-God effect becomes non-perturbatively strong. We extend a simplified treatment of EFT corrections at two-loop order from real to redshift space, making sure that the leading UV-sensitivity of both the single-hard and double-hard limit of the two-loop contributions to the power spectrum is accounted for, and featuring two free parameters for each multipole. Taking also infrared-resummation into account, we calibrate with and compare to Quijote N -body simulations for the monopole and quadrupole at redshifts $z = 0$ and $z = 0.5$. We find agreement within sample variance (at percent-level) up to $0.18h \text{ Mpc}^{-1}$ at two-loop order, compared to $0.1h \text{ Mpc}^{-1}$ at one-loop. We also investigate the role of higher-derivative corrections.

Contents

1	Introduction	1
2	Perturbation theory in redshift space	3
2.1	EFT framework	5
2.2	IR-resummation	6
3	Numerical analysis	7
3.1	Redshift $z = 0$	8
3.2	Redshift $z = 0.5$	10
3.3	Add k^4 counterterm to NLO prediction	11
4	Conclusion	12
A	Redshift-space kernels	13
B	Additional checks and supplementary results	13
B.1	Subtraction of double-hard contribution	14
B.2	Cutoff-dependence	14
B.3	Real space	15
B.4	Chi-squared	15
B.5	Add k^4 counterterm to NNLO prediction	16
B.6	Hexadecapole	17
C	Analytical results for the single- and double-hard limits	17
C.1	Single-hard EFT counterterm	17
C.2	Single-hard limit of Z_4 and Z_5	21
C.3	Double-hard limit	21

1 Introduction

Galaxy surveys mapping out the three-dimensional large-scale structure (LSS) of the Universe rely on redshift information to infer radial distances. Hence theoretical interpretation of galaxy clustering data is performed in *redshift space* rather than real space, accounting for the impact of galaxies' peculiar velocities along the line-of-sight, referred to as redshift-space distortions (RSD) [1]. This greatly complicates the theoretical modeling, but on the flip side RSD contain additional information about peculiar velocities on cosmological scales, being sensitive to the linear growth rate $f = d \ln D / d \ln a$, where $D(z)$ is the linear growth factor (e.g. [2]). Current galaxy surveys such as DESI [3] and Euclid [4] will measure RSD at unprecedented precision, yielding percent-level measurements of the growth rate [4].

On mildly non-linear scales the clustering of matter in real space can be described perturbatively within a fluid model [5], following the evolution of the lowest moments of the Boltzmann hierarchy: the density and velocity fields. Given its initial smallness, the second moment — the velocity dispersion tensor — can be neglected on very large scales. It is however well-known that non-linear evolution leads to sizable velocity dispersion, which back-reacts on mildly non-linear scales via mode-coupling [6]. Hence an accurate prescription for the dispersion tensor is required. In the effective field theory (EFT) approach, the velocity dispersion tensor is treated as a functional of the long-wavelength fields (and gradients of them), including all combinations that are allowed by symmetries, encompassing mass and momentum conservation as well as extended Galilean invariance [7]. Each contribution can be written as a product of an operator containing the fields and an unknown Wilson coefficient (frequently dubbed counterterm in this context). The latter is not predicted by the theory but rather inferred by fitting

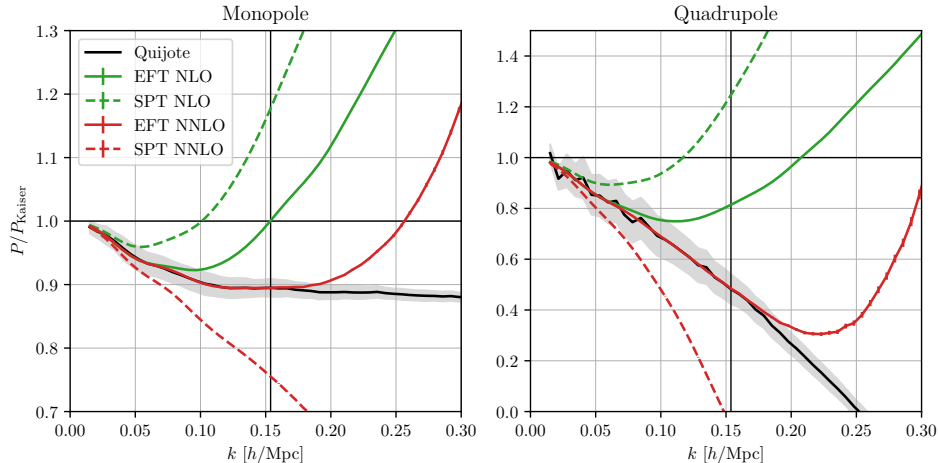


Figure 1. Perturbation theory predictions for the matter power spectrum monopole and quadrupole in redshift space, compared to Quijote N -body simulation data at redshift $z = 0$ (black). The graphs are normalized to the linear Kaiser prediction (see Eq. (2.7)). Gray bands indicate the N -body simulation uncertainty from sample variance. The green solid lines correspond to a 0-parameter NLO prediction (using the “ c_s^2 ” EFT coefficient measured at two-loop, rather than fitting it at one-loop, in order to mitigate overfitting issues at one-loop, see Sec. 3). The red solid lines show our 2-parameter NNLO results. The corresponding SPT results (no EFT corrections) are displayed with dashed lines. The vertical line indicates the pivot scale k_{max} .

to N -body simulations or marginalized over in data analysis. Although introducing additional free coefficients, the EFT approach has proven a useful alternative to exploit the full-shape information [8–14] of BOSS clustering data [2], see [15–17]. Apart from an EFT description, the velocity dispersion tensor can also be included as a dynamic variable, trading the need for free coefficients for a greater computational complexity [18, 19].

Mapping the density field to redshift space has two main effects [1, 20–22]: large-scale overdensities will look squashed along the line-of-sight due to the infalling peculiar velocity field, yielding enhanced power on large separations parallel to the line-of-sight. On the other hand, large pairwise velocities on small scales lead to distortions being elongated parallel to the line-of-sight, referred to as the “fingers-of-God” (FoG) effect [20]. The former can be adequately described in linear theory with the well-known Kaiser formula [1] and treated perturbatively at higher order. Due to its non-linear nature, the second effect presents a much greater challenge for a perturbative treatment. In particular, the distribution of pairwise velocities determining the suppression of the redshift-space power spectrum on the FoG scale $k \sim 0.2h \text{ Mpc}^{-1}$ features strongly non-Gaussian tails generated by non-linear evolution [22]. This motivates an ansatz for the suppression based on a combination of Gaussian and Lorentzian form [12, 23], encapsulating the impact of higher moments of the pairwise velocity distribution. Following instead a strictly perturbative approach, as done in this work, the mapping to redshift space involves an additional power series expansion of velocity fields, increasing the relative importance of higher loop corrections on mildly non-linear scales as compared to the power spectrum in real space. In addition, the mapping involves products of fields at the same spatial position, giving rise to contact terms, being related to the pairwise velocity moments at infinite separation [22]. Within the EFT approach these need to be renormalized by additional counterterms [24, 25] (see also [26]). A priori a strictly perturbative approach in redshift space can be expected to be in principle possible for scales up to around the FoG scale $k \lesssim 0.2h \text{ Mpc}^{-1}$.

In this work, we present the complete *two-loop* matter power spectrum in redshift space in the EFT approach, for the first time to our knowledge¹. We follow a perturbative approach complemented

¹The two-loop redshift-space power spectrum is calculated within the *GridSPT* framework in [27]. See also [28], where two-loop contributions in redshift space are discussed in the context of the TNS model [29]. We note that the latter approach does not include all terms contributing in a strict perturbative expansion of the redshift-space mapping, but instead encapsulates some of them into a finger-of-God factor that is not treated perturbatively, but replaced by a

by EFT corrections, involving the density field in redshift space up to fifth order. We compute the ultraviolet (UV) sensitivity of the redshift-space two-loop correction analytically for EdS kernels, establishing that the double-hard limit can be renormalized by the counterterms present at one-loop (as required by mass and momentum conservation). We add one extra EFT parameter for each redshift-space multipole to renormalize the single-hard limit of the two-loop correction, making the ansatz that the small-scale physics affect intermediate scales in a manner matching the UV-sensitivity of the bare theory, which has been shown to work well for the two-loop power spectrum in real space [30]. Thus, at next-to-next-to leading order (NNLO), we have two free coefficients for each multipole. After implementing infrared (IR) resummation, we calibrate and compare our predictions to Quijote N -body simulation data.

The main result of this work is displayed in Fig. 1. The perturbation theory predictions for the redshift-space monopole and quadrupole at redshift $z = 0$ at NLO and NNLO are shown, as well as the Quijote N -body simulation result. Here, we used a 0-parameter model at NLO and a 2-parameter model (for each multipole) at NNLO (for the NLO counterterms, we use the value of the corresponding EFT parameters more precisely measured at NNLO, see Sec. 3). For comparison, the SPT results are displayed with dashed lines. We find that the NLO EFT result is in agreement with the Quijote N -body data (within uncertainties from sample variance) up to $k \simeq 0.1h \text{ Mpc}^{-1}$, while adding the two-loop increases the wavenumbers with agreement to $k \simeq 0.18h \text{ Mpc}^{-1}$ at NNLO.

This work is structured as follows: in Sec. 2, we review Eulerian perturbation theory in redshift space, and outline the EFT framework we utilize. Moreover, we demonstrate the IR-resummation procedure we adopt. In Sec. 3, we fit and compare our perturbative results to Quijote N -body data, contrasting the NNLO result with various prescriptions for treating the NLO case. We conclude in Sec. 4. In App. A we describe our implementation of Z_n kernels for the matter density contrast in redshift space. We perform various tests to validate our method as well as provide some supplementary results in App. B. Finally, in App. C we present analytical expressions for the single- and double-hard limit of the two-loop power spectrum monopole and quadrupole in redshift space, as well as for the corresponding two-loop EFT corrections.

2 Perturbation theory in redshift space

In this section, we provide a brief review of Eulerian perturbation theory in redshift space, establishing the formalism and notation we use. Furthermore, we describe the EFT framework that we will utilize at two-loop order.

The distance to observed galaxies is inferred from their radial velocities, which includes contributions from both the Hubble flow, reflecting the true distance, as well as “distortions” caused by the galaxies’ peculiar velocities [1, 5, 22]. An object at position \mathbf{x} is assigned the *redshift space* coordinate

$$\mathbf{s} = \mathbf{x} - f u_z(\mathbf{x}) \hat{z}, \quad (2.1)$$

where $f = d \ln D / d \ln a$ is the growth rate, $\mathbf{u}(\mathbf{x}) = -\mathbf{v}(\mathbf{x}) / \mathcal{H} f$ denotes the (rescaled) peculiar velocity, and we have assumed that the line-of-sight is a fixed direction \hat{z} (plane-parallel approximation). By using the preservation of mass density under the coordinate transformation, one can show that the redshift space density contrast δ_s in Fourier space is given by [5]²

$$\delta_s(\mathbf{k}) = \int \frac{d^3 \mathbf{x}}{(2\pi)^3} e^{-i\mathbf{k} \cdot \mathbf{x}} e^{i f k_z u_z(\mathbf{x})} [\delta(\mathbf{x}) + f \nabla_z u_z(\mathbf{x})]. \quad (2.2)$$

Expanding the exponential function as well as the fields themselves yields the following perturbative

phenomenological suppression function.

²Neglecting contributions for which $f \nabla_z u_z(\mathbf{x}) \geq 1$.

expression

$$\begin{aligned}\delta_s(\mathbf{k}) &= \sum_{n=1}^{\infty} \int_{\mathbf{q}_1, \dots, \mathbf{q}_n} \delta_D \left(\mathbf{k} - \sum_{i=1}^n \mathbf{q}_i \right) [\delta(\mathbf{q}_1) + f\mu_1^2 \theta(\mathbf{q}_1)] \frac{(f\mu k)^{n-1}}{(n-1)!} \frac{\mu_2}{q_2} \theta(\mathbf{q}_2) \cdots \frac{\mu_n}{q_n} \theta(\mathbf{q}_n) \\ &\equiv \sum_{n=1}^{\infty} \int_{\mathbf{q}_1, \dots, \mathbf{q}_n} \delta_D \left(\mathbf{k} - \sum_{i=1}^n \mathbf{q}_i \right) Z_n(\mathbf{q}_1, \dots, \mathbf{q}_n) \delta_1(\mathbf{q}_1) \cdots \delta_1(\mathbf{q}_n),\end{aligned}\quad (2.3)$$

where we adopted the notation $\int_{\mathbf{q}} = \int d^3\mathbf{q}$. The redshift space kernels Z_n represent the perturbative expansion, and they are given up to third order as

$$Z_1(\mathbf{q}) = (1 + f\mu^2), \quad (2.4a)$$

$$Z_2(\mathbf{q}_1, \mathbf{q}_2) = F_2(\mathbf{q}_1, \mathbf{q}_2) + f\mu^2 G_2(\mathbf{q}_1, \mathbf{q}_2) + \frac{f\mu k}{2} \left[\frac{\mu_1}{q_1} (1 + f\mu_2^2) + \frac{\mu_2}{q_2} (1 + f\mu_1^2) \right], \quad (2.4b)$$

$$\begin{aligned}Z_3(\mathbf{q}_1, \mathbf{q}_2, \mathbf{q}_3) &= F_3(\mathbf{q}_1, \mathbf{q}_2, \mathbf{q}_3) + f\mu^2 G_3(\mathbf{q}_1, \mathbf{q}_2, \mathbf{q}_3) \\ &\quad + f\mu k \left[F_2(\mathbf{q}_1, \mathbf{q}_2) + f\mu_{12}^2 G_2(\mathbf{q}_1, \mathbf{q}_2) \right] \frac{\mu_3}{q_3} + f\mu k (1 + f\mu_1^2) \frac{\mu_{23}}{q_{23}} G_2(\mathbf{q}_2, \mathbf{q}_3) \\ &\quad + \frac{(f\mu k)^2}{2} (1 + f\mu_1^2) \frac{\mu_2 \mu_3}{q_2 q_3} + \text{perm.}\end{aligned}\quad (2.4c)$$

In the above expressions, $\mathbf{k} = \sum_i \mathbf{q}_i$, $\mu = \mathbf{k} \cdot \hat{z}/k$, $\mu_i = \mathbf{q}_i \cdot \hat{z}/q_i$ and F_n and G_n denote the usual (symmetrized) density contrast and velocity divergence kernels, respectively. For brevity, we have omitted the explicit contributions from two permutations of wavenumber arguments in the second and third line of the expression for Z_3 . Note that the linear kernel is exactly the Kaiser prediction. In this work we use kernels up to Z_5 . A general formula for the n -th order redshift-space kernel is given in App. A. We note that the well-known constraints from mass and momentum conservation as well as Galilean invariance translate into the properties $Z_n(\mathbf{q}_1, \dots, \mathbf{q}_{n-2}, \mathbf{q}, -\mathbf{q}) \propto k^2/q^2$ for $q \gg k$ and

$$Z_{n+1}(\mathbf{q}_1, \dots, \mathbf{q}_n, \mathbf{q}) \rightarrow \frac{\mathbf{k} \cdot \mathbf{q} + f k q \mu \mu_q}{(n+1)q^2} Z_n(\mathbf{q}_1, \dots, \mathbf{q}_n), \quad (2.5)$$

in the limit $q \rightarrow 0$, respectively. Here $\mu_q = (\mathbf{q} \cdot \hat{z})/q$. The former relation is instrumental for the construction of the EFT corrections, and implies that they are largely analogous as in real space, see Sec. 2.1. The latter property ensures cancellation of contributions to loop integrals that are enhanced for small loop wavenumber, which can be made explicit by the same algorithm as described in [31, 32]. It also underlies the IR-resummation in redshift space [33], see Sec. 2.2. In this work, our primary focus is on the perturbative treatment of the mapping from real to redshift space, therefore we do not consider bias, i.e. we model the total matter density in redshift space.

Ultimately, we are interested in loop corrections to the power spectrum multipoles in redshift space. To illustrate how we can numerically evaluate the loop integrals as well as how we subsequently renormalize them, it is useful to define the L -loop *integrand* p_L in redshift space as

$$P_s^{L\text{-loop}}(k, \mu) = \int_{\mathbf{q}_1, \dots, \mathbf{q}_L} p_{s,L}(\mathbf{k}, \mu, \mathbf{q}_1, \dots, \mathbf{q}_L) P_0(q_1) \cdots P_0(q_L), \quad (2.6)$$

where

$$\begin{aligned}p_{s,L=0}(\mathbf{k}, \mu) &= Z_1(\mathbf{k})^2 P_0(k), \\ p_{s,L=1}(\mathbf{k}, \mu, \mathbf{q}_1) &= 6Z_3(\mathbf{k}, \mathbf{q}_1, -\mathbf{q}_1) Z_1(\mathbf{k}) P_0(k) + 2Z_2(\mathbf{k} - \mathbf{q}_1, \mathbf{q}_1)^2 P_0(|\mathbf{k} - \mathbf{q}_1|), \\ p_{s,L=2}(\mathbf{k}, \mu, \mathbf{q}_1, \mathbf{q}_2) &= 6Z_3(\mathbf{k} - \mathbf{q}_1 - \mathbf{q}_2, \mathbf{q}_1, \mathbf{q}_2)^2 P_0(|\mathbf{k} - \mathbf{q}_1 - \mathbf{q}_2|) \\ &\quad + (30Z_5(\mathbf{k}, \mathbf{q}_1, -\mathbf{q}_1, \mathbf{q}_2, -\mathbf{q}_2) Z_1(\mathbf{k}) + 9Z_3(\mathbf{k}, \mathbf{q}_1, -\mathbf{q}_1) Z_3(\mathbf{k}, \mathbf{q}_2, -\mathbf{q}_2)) P_0(k) \\ &\quad + 12Z_4(\mathbf{k} - \mathbf{q}_1, \mathbf{q}_1, \mathbf{q}_2, -\mathbf{q}_2) Z_2(\mathbf{k} - \mathbf{q}_1, \mathbf{q}_1) P_0(|\mathbf{k} - \mathbf{q}_1|) \\ &\quad + 12Z_4(\mathbf{k} - \mathbf{q}_2, \mathbf{q}_2, \mathbf{q}_1, -\mathbf{q}_1) Z_2(\mathbf{k} - \mathbf{q}_2, \mathbf{q}_2) P_0(|\mathbf{k} - \mathbf{q}_2|).\end{aligned}\quad (2.7)$$

We use the freedom to relabel the integration variables to ensure $p_{s,2}(\mathbf{k}, \mu, \mathbf{q}_1, \mathbf{q}_2) = p_{s,2}(\mathbf{k}, \mu, \mathbf{q}_2, \mathbf{q}_1)$, which is irrelevant for the two-loop result, but important for the definition of the two-loop EFT correction discussed below. For numerical evaluation we in addition apply the rewritings as in [31, 32] to ensure cancellation of IR enhanced terms at the integrand level as mentioned above. The case $L = 0$ corresponds to the linear Kaiser spectrum, $0\text{-loop} \equiv \text{lin}$, with no loop integration.

The power spectrum multipoles are projections onto Legendre polynomials $\mathcal{P}_l(\mu)$:

$$P_l^{L\text{-loop}}(k) = \frac{2l+1}{2} \int_{-1}^1 d\mu \mathcal{P}_l(\mu) P_s^{L\text{-loop}}(k, \mu). \quad (2.8)$$

We perform the loop integrals as well as the μ -integral above numerically using Monte Carlo integration. Hence, for each sample of the integrand, we evaluate the kernels that appear at that order, which at two-loop includes kernels up to Z_5 . To compute the kernels efficiently, we develop an extension of the algorithm for the F_n and G_n kernels from Ref. [32], that in a recursive manner perturbatively expands the various factors of the first line of Eq. (2.3). The algorithm is explained in more detail in App. A.

2.1 EFT framework

It is well-known that SPT breaks down on even mildly non-linear scales and the higher loop corrections suffer from large, spurious contributions from the UV [32, 34]. To address this issue, within the EFT approach “counterterms” are incorporated that systematically capture the impact of small scales on intermediate scales, renormalizing the theory and restoring convergence of the perturbation theory [7, 35]. In principle all counterterms allowed by the symmetries of the problem (statistical homogeneity and isotropy, mass and momentum conservation, extended Galilean invariance) should be included, accompanied by free coefficients that are not predicted by the EFT. Moreover, the mapping from real space to redshift space involves products of coarse-grained fields at the same point in space (contact terms) [22], which in the EFT need to be renormalized by additional counterterms [24, 25].

In practice, there are substantial degeneracies between counterterms and one can only fit certain combinations of them accurately. Furthermore, including many parameters increases the risk of overfitting when comparing the EFT to data/simulations. For the two-loop power spectrum (in real space), a two-parameter ansatz for the EFT corrections has been shown to work well in practice [30, 36]. We briefly discuss this scheme in the following and refer the reader to the quoted references for a more thorough discussion. The renormalized two-loop power spectrum in real space reads

$$P_{\text{NNLO}}^{\text{ren.}}(k) = P^{\text{lin}}(k) + P^{1\text{-loop}}(k; \Lambda) + \bar{P}^{2\text{-loop}}(k; \Lambda) + \gamma_1(\Lambda) k^2 P^{\text{lin}}(k) + \gamma_2(\Lambda) \bar{P}_{\text{sh}}^{2\text{-loop}}(k; \Lambda), \quad (2.9)$$

where $P^{\text{lin}} \equiv P_0$ is the linear power spectrum and $P^{L\text{-loop}}(\Lambda)$ is the (bare) L -th loop correction evaluated with cutoff Λ . The bar notation will be explained shortly. The EFT parameters are denoted by γ_1 and γ_2 , with the former representing the usual “ c_s^2 ” correction to the sound speed of the fluid present already at one-loop. The latter multiplies the *single-hard* two-loop contribution, defined implicitly as follows:

$$\begin{aligned} P^{2\text{-loop}}(k; \Lambda) &\xrightarrow{q_1 \gg k} 3 \int_{\mathbf{q}_2}^{\Lambda} \int \frac{d\Omega_{q_1}}{4\pi} \left[q_1^2 \lim_{q_1 \rightarrow \infty} p_2(\mathbf{k}, \mathbf{q}_1, \mathbf{q}_2) P_0(q_2) \right] \frac{4\pi}{3} \int^{\Lambda} dq_1 P_0(q_1) \\ &\equiv \frac{1}{2} P_{\text{sh}}^{2\text{-loop}}(k; \Lambda) \sigma_d^2(\Lambda), \end{aligned} \quad (2.10)$$

where p_2 is the two-loop *integrand* in real space and $d\Omega_{q_1}$ is the differential solid angle of \mathbf{q}_1 (see App. C). The above factorization is valid at leading order in k^2/q_1^2 in the limit where q_1 is hard; due to the $1/q_1^2$ -scaling of the kernels in the limit guaranteed by momentum conservation, the bracket above is *independent* of \mathbf{q}_1 , and we could factorize out the displacement dispersion $\sigma_d^2 \equiv 4\pi/3 \int dq P_0(q)$. The factor 1/2 in the final expression is present so that the definition of the single-hard contribution $P_{\text{sh}}^{2\text{-loop}}$ also incorporates the equivalent limit in which $q_2 \gg k, q_1$. Thus, this ansatz for the two-loop counterterm amounts to assuming that the EFT corrects the UV in a universal manner dictated by

the UV-sensitivity of SPT. In other words, we assume that we can renormalize the two-loop correction by shifting the value of the displacement dispersion $\sigma_d^2 \rightarrow \sigma_d^2 + \gamma_2$.

Finally, the double-hard limit $q_1, q_2 \gg k$ of the two-loop correction is renormalized by the γ_1 -term introduced already at one-loop. We opt for a renormalization scheme where γ_1 incorporates the correction of the hard limit of the one-loop as well as the actual impact of short-scale physics (the “finite” contribution), using the freedom to shift γ_1 such that the double-hard contribution of the two-loop correction exactly cancels. In practice, this means that we subtract the double hard contributions from the two-loop correction $P^{2\text{-loop}}$ as well as from the single-hard two-loop counterterm $\bar{P}_{\text{sh}}^{2\text{-loop}}$. This operation is indicated by bars in Eq. (2.9). See App. C for analytic expressions for the single- and double-hard limits of the two-loop. We stress that this choice of subtracting the double-hard contribution has no impact on the results, except for a shift in γ_1 .

Next, we extend this EFT setup to redshift space. We renormalize each multipole l by the extension of the two-parameter ansatz described above,

$$P_{l,\text{NNLO}}^{\text{ren.}}(k) = P_l^{\text{lin}}(k) + P_l^{1\text{-loop}}(k; \Lambda) + \bar{P}_l^{2\text{-loop}}(k; \Lambda) + \gamma_1(\Lambda)k^2 P_l^{\text{lin}}(k) + \gamma_2(\Lambda)\bar{P}_{l,\text{sh}}^{2\text{-loop}}(k; \Lambda), \quad (2.11)$$

where P_l^{lin} is the Kaiser prediction and the loop corrections are given by Eqs. (2.7) and (2.8). We define the single-hard two-loop counterterm analogously to Eq. (2.10),

$$P_{l,\text{sh}}^{2\text{-loop}}(k; \Lambda) = 2 \times 3 \times \frac{2l+1}{2} \int_{-1}^1 d\mu \mathcal{P}_l(\mu) \int_{\mathbf{q}_2} \int \frac{d\Omega_{\mathbf{q}_1}}{4\pi} \left[q_1^2 \lim_{q_1 \rightarrow \infty} p_{s,2}(\mathbf{k}, \mu, \mathbf{q}_1, \mathbf{q}_2) P_0(q_2) \right], \quad (2.12)$$

including a factor 2 to account for the equivalent limit in which \mathbf{q}_2 is hard. Hence, we introduce two EFT parameters for each multipole in redshift space. We give explicit expressions for the single-hard EFT correction $\bar{P}_{l,\text{sh}}^{2\text{-loop}}(k; \Lambda)$ in App. C, that effectively amount to one-loop integrals. Furthermore, we demonstrate in App. B.2 that this prescription yields cutoff-independent predictions for the multipoles. In practice, we find it convenient to compute the single-hard limit numerically by fixing one wavenumber to a large value, $q_1 = 10h \text{ Mpc}^{-1}$, in the two-loop evaluation.

Note that in Eq. (2.11) we defined EFT parameters independently for each multipole, in contrast to typical conventions in the EFT literature, e.g. [16, 37], where the counterterms are defined in redshift space with certain μ -dependencies. Given the numerical complexity of integrating the two-loop single-hard counterterm over μ , we opt to parametrize the counterterms by their projection onto Legendre polynomials, avoiding the need to perform the integral repeatedly when fitting the EFT parameters. This also allows us to treat each multipole separately. We stress that the approaches are equivalent when considering multipoles up to at most $\ell = 4$, and simply related by a change of basis in μ -space.

2.2 IR-resummation

To properly model the BAO wiggles in the power spectrum we need to include the effect of large displacements. These are not adequately modeled in SPT; however, how to resum their impact on the BAOs is well-understood [33, 38–43]. After separating out the BAO wiggles (w) from the broadband (nw) linear spectrum in real space, $P^{\text{lin}} = P_{\text{nw}} + P_{\text{w}}$ (for the numerical analysis in Sec. 3 we perform this splitting using the algorithm of [37, 44]), one defines the IR damping factor [43]

$$\Sigma^2(z) = \frac{4\pi}{3} \int_0^{k_s} dq P_{\text{nw}}(q) \left[1 - j_0\left(\frac{q}{k_{\text{osc}}}\right) + 2j_2\left(\frac{q}{k_{\text{osc}}}\right) \right], \quad (2.13)$$

where $k_{\text{osc}} = h/(110 \text{ Mpc})$ is the wavenumber of the BAO oscillations, k_s is the separation scale between short and long modes in the resummation and j_n is the spherical Bessel function. In redshift space we need the additional damping factor [33]

$$\delta\Sigma^2(z) = 4\pi \int_0^{k_s} dq P_{\text{nw}}(q) j_2\left(\frac{q}{k_{\text{osc}}}\right), \quad (2.14)$$

yielding the following total, anisotropic damping factor in redshift space (related to Eq. (2.5)):

$$\Sigma_{\text{tot}}^2(z, \mu) = (1 + f(z)\mu^2(2 + f(z)))\Sigma^2(z) + f^2(z)\mu^2(\mu^2 - 1)\delta\Sigma^2(z). \quad (2.15)$$

The IR-resummed perturbative contributions to the power spectrum then reads

$$P_{s,\text{LO}}^{\text{IR}}(k, \mu) = (Z_1(k, \mu))^2 \left(P_{\text{nw}}(k) + e^{-k^2 \Sigma_{\text{tot}}^2(\mu)} P_{\text{w}}(k) \right), \quad (2.16\text{a})$$

$$P_{s,\text{NLO}}^{\text{IR}}(k, \mu) = (Z_1(k, \mu))^2 \left(P_{\text{nw}}(k) + (1 + k^2 \Sigma_{\text{tot}}^2(\mu)) e^{-k^2 \Sigma_{\text{tot}}^2(\mu)} P_{\text{w}}(k) \right) \\ + P_s^{1\text{-loop}} \left[P_{\text{nw}}(q) + e^{-q^2 \Sigma_{\text{tot}}^2(\mu)} P_{\text{w}}(q) \right], \quad (2.16\text{b})$$

$$P_{s,\text{NNLO}}^{\text{IR}}(k, \mu) = (Z_1(k, \mu))^2 \left(P_{\text{nw}}(k) + \left(1 + k^2 \Sigma_{\text{tot}}^2(\mu) + \frac{1}{2} (k^2 \Sigma_{\text{tot}}^2(\mu))^2 \right) e^{-k^2 \Sigma_{\text{tot}}^2(\mu)} P_{\text{w}}(k) \right) \\ + P_s^{1\text{-loop}} \left[P_{\text{nw}}(q) + (1 + q^2 \Sigma_{\text{tot}}^2(\mu)) e^{-q^2 \Sigma_{\text{tot}}^2(\mu)} P_{\text{w}}(q) \right] \\ + \bar{P}_s^{2\text{-loop}} \left[P_{\text{nw}}(q) + e^{-q^2 \Sigma_{\text{tot}}^2(\mu)} P_{\text{w}}(q) \right], \quad (2.16\text{c})$$

where the notation $P_s^{L\text{-loop}}[X]$ indicates that X is the power spectrum entering the integrand of the loop corrections. Note that the additional terms $\sim k^2 \Sigma^2$ and $\sim (k^2 \Sigma^2)^2$ correct for the overcounting of IR contributions already included in the loop integrals.

In summary, the renormalized and IR-resummed two-loop power spectrum in redshift space is

$$P_{l,\text{NNLO}}^{\text{IR,ren.}}(k) = \frac{2l+1}{2} \int_{-1}^1 d\mu \mathcal{P}_l(\mu) P_{s,\text{NNLO}}^{\text{IR}}(k, \mu) + \gamma_1(\Lambda) k^2 P_l^{\text{lin}}(k) + \gamma_2(\Lambda) \bar{P}_{l,\text{sh}}^{2\text{-loop}}(k; \Lambda), \quad (2.17)$$

where the last two terms are the EFT corrections discussed above, but evaluated using $P_0(q) = P_{\text{nw}}(q) + e^{-q^2 \Sigma^2(\mu)} P_{\text{w}}(q)$ as input spectrum. The NLO prediction is computed analogously, but including only the γ_1 term.

3 Numerical analysis

In this section we compare the two-loop matter power spectrum in redshift space, including EFT corrections and IR-resummation, to numerical N -body simulation results from the Quijote suite [45]. The simulations feature 500 realizations of $(512)^3$ CDM particles in a cubic box of size $(1 \text{ Gpc}/h)^3$ with pair-fixed initial conditions which have reduced cosmic variance. The cosmological parameters are $\Omega_m = 0.3175$, $\Omega_b = 0.049$, $h = 0.6711$, $n_s = 0.9624$ and $\sigma_8 = 0.834$. We use the EdS-approximation for the matter kernels (see e.g. [36, 46] for analyses of the impact of the EdS-approximation on the two-loop power spectrum in real space). The loop integrals are cutoff at $\Lambda = 1h \text{ Mpc}^{-1}$, however, as we check explicitly in App. B.2, the EFT prescription ensures that our results do not depend on this choice. We present results for the monopole $\ell = 0$ and quadrupole $\ell = 2$. A presentation of the hexadecapole $\ell = 4$ is left to Appendix B.6 due to it not being estimated as well by the simulations. Furthermore we consider redshifts $z = 0$ and $z = 0.5$ in Sec. 3.1 and Sec. 3.2, respectively.

We determine the EFT coefficients γ_1 and γ_2 defined in Eq. (2.17) by fitting the perturbative result to the corresponding simulation output, taking all k -bins up to some maximal wavenumber k_{max} into account. In practice, we minimize the function

$$\chi^2(k_{\text{max}}) \equiv \sum_{k_i \leq k_{\text{max}}} \frac{1}{\sigma_{k_i}^2} \left(P_{l,\text{NNLO}}^{\text{IR,ren.}}(k_i) - P_l^{\text{Quijote}}(k_i) \right)^2, \quad (3.1)$$

where $\sigma_{k_i}^2$ is determined from the variance of the 500 realizations provided in the Quijote simulation suite. Throughout the analysis, the first k -bin of the Quijote redshift-space data vector is removed, which due to discreteness effects is inaccurate. We reiterate that we perform the EFT fit independently for each multipole.

In order to compare our two-loop results to those at one-loop, we consider various different possibilities for the latter, varying in the number of free EFT parameters allowed in the fit. The EFT

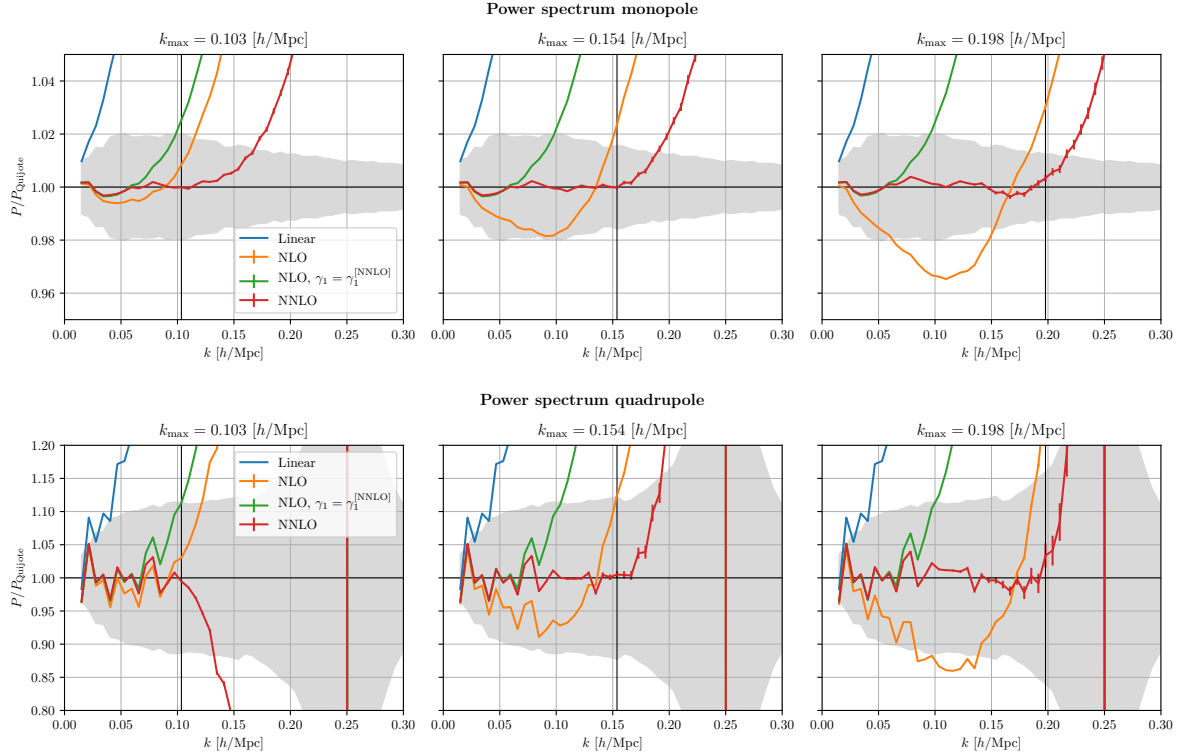


Figure 2. Predictions for the monopole (upper panel) and quadrupole (lower panel) contributions to the power spectrum in redshift space at $z = 0$, normalized to the Quijote result. We display the linear (blue), NLO 0-parameter (green), NLO 1-parameter (orange) and NNLO (red) predictions using three pivot scales $k_{\max} \simeq 0.1, 0.15$ and $0.2 h \text{ Mpc}^{-1}$ from left to right. The Quijote uncertainty due to sample variance is indicated by the gray shading, and errorbars on the theory predictions mark the uncertainty from the numerical loop integration.

schemes can be summarized as follows:

NLO	$\{\gamma_1\}$	one-loop, 1-parameter,
NLO, $\gamma_1 = \gamma_1^{\text{NNLO}}$	$\{\emptyset\}$	one-loop, 0-parameter with γ_1 fixed from NNLO fit,
NLO + k^4	$\{\gamma_1, \gamma_{k^4}\}$	one-loop, 2-parameter, including proxy counterterm $\gamma_{k^4} k^4 P_l^{\text{lin}}(k)$,
NNLO	$\{\gamma_1, \gamma_2\}$	two-loop, 2-parameter.

The first scheme is the typical one-loop EFT prescription, which we find to be prone to overfitting already for moderate values of k_{\max} due to the limited range of validity of the one-loop approximation. Following [36], we therefore also present NLO results for which the leading EFT coefficient γ_1 is taken from the best-fit of the NNLO result. Alternatively, one could limit the range of k_{\max} at NLO compared to NNLO, but we opt for the former possibility in order to exhibit the dependence on k_{\max} at NLO as compared to NNLO. Finally, in Sec. 3.3, we also consider the option of adding a second EFT term to the NLO result, as this scheme has been used in various analyses [15, 47–49].

3.1 Redshift $z = 0$

Our result for the NNLO power spectrum in redshift space at $z = 0$ is shown in Fig. 2 for the monopole (upper row) and quadrupole (lower row), and three values of k_{\max} , respectively. The power spectra are normalized to those obtained from the Quijote simulation, with gray shaded areas bracketing its uncertainty. As expected, the simulation results are subject to larger statistical fluctuations for the

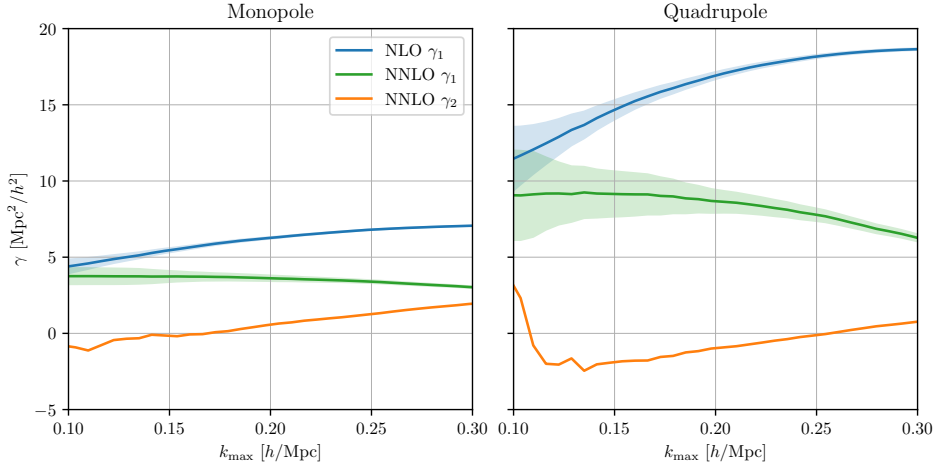


Figure 3. Measured EFT parameters as a function of pivot scale k_{\max} , within the 1-parameter NLO (blue) and 2-parameter NNLO (green and orange) EFT models, for the monopole (left) and quadrupole (right), all at $z = 0$. Shaded regions indicate 1σ uncertainty from the fit.

quadrupole, with its relative size becoming particularly large close to the scale where it changes sign at around $0.25h \text{ Mpc}^{-1}$.

For our perturbative analysis we limit ourselves to the regime below both the FoG and non-linear scales. The former can be identified with the scale for which $k^2 f^2 \sigma_v^2 = 1$, where $\sigma_v^2 \equiv 1/3 \int_{\mathbf{q}} P_{\theta\theta}(q)/q^2$ is related to the variance of the velocity power spectrum [22]. Using the linear spectrum to compute the variance yields $k_{\text{FoG}}(z = 0) = 0.198h \text{ Mpc}^{-1}$ for the considered cosmology. As well-known this scale is somewhat below the usual non-linear scale, $k_{\text{NL}}(z = 0) = 0.31h \text{ Mpc}^{-1}$, defined by the wavenumber for which the variance of the (linear) density field smoothed on that scale is equal to unity.

We find that the NNLO power spectrum is in very good agreement with Quijote results for all $k \lesssim k_{\max}$ for both the monopole and quadrupole when choosing $k_{\max} \simeq 0.1$ or $0.15h \text{ Mpc}^{-1}$ (red lines in left and middle columns in Fig. 2, respectively). The agreement extends to wavenumbers somewhat above the pivot scale particularly for the monopole. For the largest pivot scale $k_{\max} \simeq 0.2h \text{ Mpc}^{-1}$ considered in our analysis (red line in right column in Fig. 2) we observe a rapid degradation of the agreement between NNLO and simulation results for $k > 0.2h \text{ Mpc}^{-1}$, in accordance with the approach of the FoG scale. Nevertheless, the EFT model is still able to describe the Quijote data at smaller wavenumbers for both the monopole and quadrupole. Overall, taking the middle pivot scale as fiducial choice, we find agreement within sample uncertainty from the Quijote data up to around $k \leq 0.18h \text{ Mpc}^{-1}$ at NNLO.

In contrast, the range of validity of the corresponding NLO predictions is more limited. For the standard 1-parameter NLO model, it is obvious that the fit to simulation data leads to a significant scale-dependent deviation for $k_{\max} \simeq 0.15$ and $0.2h \text{ Mpc}^{-1}$, that we interpret as a sign of overfitting (orange lines in middle and right columns in Fig. 2, respectively). For comparison we therefore also display the 0-parameter NLO model described above, for which the EFT parameter γ_1 is taken from the NNLO fit result (green lines). Due to the larger range of validity of the NNLO prediction, the potential impact of overfitting is mitigated in this way. We therefore consider the 0-parameter NLO result more appropriate for large k_{\max} . For the smallest pivot scale $k_{\max} \simeq 0.1h \text{ Mpc}^{-1}$, the 0- and 1-parameter NLO results are more close to each other, signaling that overfitting is less of an issue for this choice (orange and green lines in left column of Fig. 2). When excluding the setups that are obviously affected by overfitting, the range of agreement between NLO and Quijote within uncertainties lies around $0.08 - 0.12h \text{ Mpc}^{-1}$ depending on the choice of pivot scale, multipole and 0- versus 1-parameter model. For an unbiased comparison to NNLO we adopt the same pivot scale $k_{\max} \simeq 0.15h \text{ Mpc}^{-1}$ and the 0-parameter model as fiducial choice, for which we find agreement

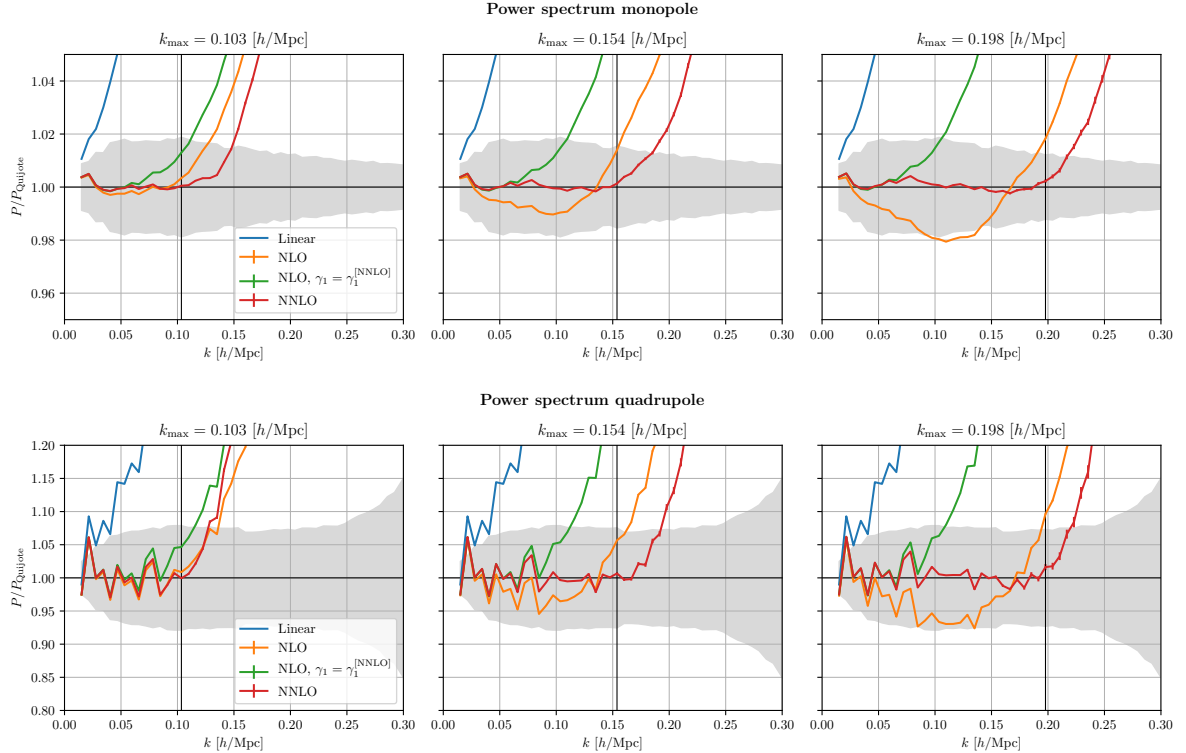


Figure 4. Same as Fig. 2 for redshift $z = 0.5$.

between NLO and Quijote data for $k \leq 0.1h \text{ Mpc}^{-1}$.

In addition to the power spectra, it is also instructive to investigate the dependence of the best-fit EFT parameters on k_{max} , shown in Fig. 3. Within the validity range, one expects the EFT parameters to be approximately independent of k_{max} , which is the case at NNLO for pivot wavenumbers below the FoG scale (green and orange lines). Interestingly, the second EFT parameter γ_2 is almost compatible with being zero over a wide range. Note that it can only be determined reliably when going to moderately large k_{max} values, since the corresponding single-hard EFT correction is highly suppressed for low k values, explaining the large uncertainty region for γ_2 in Fig. 3. The γ_1 parameter is significantly larger as compared to the real space power spectrum [30] (see also App. B.3). This may be expected due to EFT corrections setting in at the FoG instead of the non-linear scale. Finally, we observe a significant scale-dependence of γ_1 obtained within the 1-parameter NLO model, particularly for the quadrupole (blue lines in Fig. 3). This can be taken as another indication that the validity range of the 1-parameter NLO result is rather limited.

Altogether, we find that going from NLO to NNLO extends the range of agreement with Quijote simulation data including sampling uncertainty for the monopole and quadrupole from $k \simeq 0.1h \text{ Mpc}^{-1}$ to $k \simeq 0.18h \text{ Mpc}^{-1}$ at $z = 0$.

3.2 Redshift $z = 0.5$

For completeness, we show the NLO and NNLO results at redshift $z = 0.5$ in Fig. 4, for the same analysis choices as in the previous section. As is well-known, the FoG scale is almost unchanged compared to $z = 0$, $k_{\text{FoG}}(z = 0.5) = 0.220h \text{ Mpc}^{-1}$, due to the counteracting effect of a smaller growth factor $D(a)$ but a larger growth rate $f(a)$. Thus, even though the non-linear scale $k_{\text{NL}}(z = 0.5) = 0.47h \text{ Mpc}^{-1}$ is around 50% larger compared to $z = 0$, a similar range of validity of the perturbative EFT model is expected in redshift space at both redshift values.

Our numerical results largely confirm this expectation, and feature similar properties as observed for $z = 0$. In particular, the NNLO result shows very good agreement with Quijote data up to the

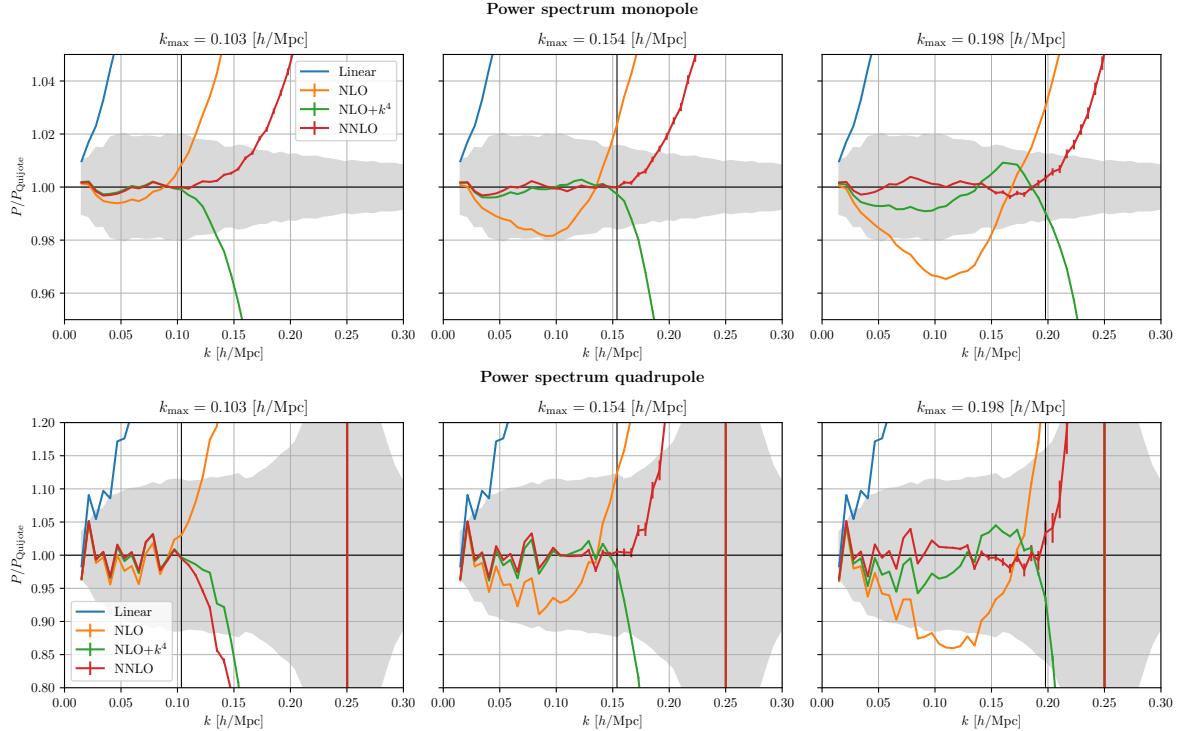


Figure 5. Impact of introducing a proxy $k^4 P_l^{\text{lin}}(k)$ counterterm at NLO. Theoretical predictions at $z = 0$ for the monopole and quadrupole normalized to Quijote N -body data are shown. The green line corresponds to the NLO prediction including a $k^4 P_l^{\text{lin}}(k)$ counterterm (2 free parameters in total), and the 1-parameter NLO as well as the NNLO results are displayed for comparison. Gray shadings indicate Quijote uncertainty, and errorbars mark uncertainty from numerical loop integration.

respective pivot scales, while the 1-parameter NLO models suffers from overfitting for $k_{\text{max}} \simeq 0.15$ and $0.2h \text{ Mpc}^{-1}$. Adopting therefore the 0-parameter NLO model for comparison, and the same fiducial pivot scale as at $z = 0$ (i.e. the middle one), we find agreement within Quijote uncertainty for the monopole and quadrupole up to $0.11h \text{ Mpc}^{-1}$ at NLO, and up to $0.18h \text{ Mpc}^{-1}$ at NNLO.

3.3 Add k^4 counterterm to NLO prediction

To account for the FoG effect within the EFT setup, it has been argued that the one-loop result for the power spectrum in redshift space can be improved by allowing for an extra additive term scaling as the product of k^4 times the linear spectrum, which can be viewed as a higher-derivative correction to the common k^2 term [15, 47, 48]. In order to assess the impact of adding this correction at NLO as compared to our NNLO results, we consider a 2-parameter NLO model in this section. In particular, relative to the 1-parameter NLO power spectrum we allow for an additional correction term $k^4 P_l^{\text{lin}}(k)$, with its prefactor being a second free EFT parameter for each multipole. We note that this is slightly more general than the template from [15, 48], where the magnitude of this correction for the monopole is correlated to that for the quadrupole. This generalization is justified within the EFT context as one expects several corrections at order k^4 , differing in their μ -dependence. We thus treat the EFT corrections to the monopole and to the quadrupole independently from each other in our analysis.

We show the result for the 2-parameter NLO model in Fig. 5 (green lines), and also the previous 1-parameter NLO (orange) and 2-parameter NNLO (red) for comparison. Adding the k^4 term notably improves the agreement of the NLO prediction with Quijote data, especially at pivot scales $k_{\text{max}} \simeq 0.1$ and $0.15h \text{ Mpc}^{-1}$. However, for $k_{\text{max}} \simeq 0.2h \text{ Mpc}^{-1}$ the NNLO result is markedly closer to Quijote than the 2-parameter NLO fit, indicating that the latter is entering the overfitting regime. Nevertheless, it is interesting that the improvement from including two-loop corrections can be somewhat

mimicked by the 2-parameter NLO model for $k \lesssim 0.15h \text{ Mpc}^{-1}$. When using scales beyond that and aiming at (sub-)percent accuracy, the inclusion of the NNLO result is still warranted.

Finally, one may wonder about the impact of adding an extra k^4 -term at NNLO, which would then feature three EFT parameters. We checked that this does not yield any improvement as compared to our fiducial 2-parameter NNLO result, and is therefore an unnecessary complication (see App. B.5 for details).

4 Conclusion

In this work we presented the matter power spectrum in redshift space including two-loop corrections. We followed a strictly perturbative approach complemented by EFT corrections, that can in principle be expected to be applicable up to scales $k \lesssim 0.2h \text{ Mpc}^{-1}$ beyond which non-perturbative FoG suppression sets in. In our work we extended the two-loop scheme proposed in [30] from real to redshift space. In particular, we add an extra EFT correction term for each multipole moment of the power spectrum, which accounts for the UV-sensitivity of the two-loop contribution when one of the loop wavenumbers becomes large (single-hard limit). The double-hard limit can be renormalized by the same $k^2 P_l^{\text{lin}}(k)$ correction included already at one-loop, as expected. In total, this leads to two free parameters for each of the multipoles we considered, specifically the monopole and quadrupole.

We performed various numerical and analytical checks to confirm the validity of the setup, and incorporated also IR-resummation. The NNLO result was calibrated with and compared to Quijote N -body simulation data for $z = 0$ and $z = 0.5$. At NNLO we find that the EFT parameters are stable against variation of the maximal wavenumber included in the fit for $k_{\text{max}} \lesssim 0.2h \text{ Mpc}^{-1}$, showing no sign of overfitting. In contrast, when using the NLO result to determine the $k^2 P_l^{\text{lin}}(k)$ correction, we find a strong scale-dependence of the best-fit coefficient within the range $k_{\text{max}} \gtrsim 0.1h \text{ Mpc}^{-1}$ allowed by N -body data. In addition, the k -dependence of the NLO result determined in this way shows indications of overfitting. We therefore opted to use the $k^2 P_l^{\text{lin}}(k)$ correction determined at NNLO for our fiducial NLO setup as well. We then find that the NLO result is in agreement with Quijote data for the monopole and quadrupole at $z = 0$ until $k \simeq 0.1h \text{ Mpc}^{-1}$. Adding the NNLO correction significantly extends the range of agreement to $k \simeq 0.18h \text{ Mpc}^{-1}$. We find a similar improvement from $k \simeq 0.11h \text{ Mpc}^{-1}$ at NLO to $k \simeq 0.18h \text{ Mpc}^{-1}$ at NNLO for redshift $z = 0.5$. This is consistent with the FoG scale being around $0.2h \text{ Mpc}^{-1}$ for both redshifts within the Λ CDM cosmology adopted in this work.

Finally, we investigated also the option proposed in [15] to add a higher-derivative correction. We considered terms of the form $k^4 P_l^{\text{lin}}(k)$, with an extra free parameter for each multipole, being slightly more general than the ansatz from [15]. At NNLO, adding this higher-derivative term does not lead to any changes compared to our fiducial setup, and we therefore omit it. However, at NLO this additional freedom can bring the result closer to N -body data for $k \lesssim 0.15h \text{ Mpc}^{-1}$. Nevertheless, especially when pushing to scales $k_{\text{max}} \simeq 0.2h \text{ Mpc}^{-1}$ the fiducial NNLO result is still in very good agreement with Quijote data while the NLO result deviates significantly even when allowing for two free parameters ($k^2 P_l^{\text{lin}}(k)$ and $k^4 P_l^{\text{lin}}(k)$ terms) for each multipole for the latter.

We provide details on our implementation of redshift-space kernels as well as complementary results, including analytical expressions for the two-loop EFT correction to the monopole and quadrupole power spectrum, in the appendices, intended for convenient usage in future works.

Acknowledgements

We thank Roman Scoccimarro for insightful discussions and Francisco Villaescusa-Navarro and Oliver Philcox for helpful comments on using the redshift-space power spectra from the Quijote simulation suite. We acknowledge support by the ANR Project COLSS (ANR-21-CE31-0029, France) and by the DFG Collaborative Research Institution Neutrinos and Dark Matter in Astro- and Particle Physics (SFB 1258).

A Redshift-space kernels

In this appendix we write down a general formula for the redshift-space kernels and briefly discuss the algorithm we employ to evaluate it for a given set of wavevectors. At n -th order, the redshift-space kernel (defined implicitly in Eq. (2.3)) can be written as

$$Z_n(\mathbf{q}_1, \dots, \mathbf{q}_n) = A_n(\mathbf{q}_1, \dots, \mathbf{q}_n) + \sum_{m=1}^{n-1} A_m(\mathbf{q}_1, \dots, \mathbf{q}_m) \sum_{p=1}^{n-m} \frac{(f\mu k)^p}{p!} B_{n-m}^{(p)}(\mathbf{q}_{m+1}, \dots, \mathbf{q}_n), \quad (\text{A.1})$$

where $\mathbf{k} = \sum_{i=1}^n \mathbf{q}_i$ and $\mu = \mathbf{k} \cdot \hat{z}/k$. We defined A_m as a shorthand notation for the m -th order perturbative expansion of the square bracket of the first line in Eq. (2.3):

$$A_m(\mathbf{q}_1, \dots, \mathbf{q}_m) = F_m(\mathbf{q}_1, \dots, \mathbf{q}_m) + f\mu_{1\dots m}^2 G_m(\mathbf{q}_1, \dots, \mathbf{q}_m), \quad (\text{A.2})$$

where $\mu_{1\dots m} = \mathbf{q}_{1\dots m} \cdot \hat{z}/q_{1\dots m}$ and $\mathbf{q}_{1\dots m} = \sum_{i=1}^m \mathbf{q}_i$. The p -sum counts contributions with p factors of velocity kernels (arising from the expansion of the exponential in Eq. (2.2)). Hence, $B_m^{(p)}$ is defined as the sum of all such terms at m -th order in perturbation theory with p factors of velocity kernels, which can more precisely be written recursively as

$$B_m^{(p)}(\mathbf{q}_1, \dots, \mathbf{q}_m) = \begin{cases} \sum_{l=p-1}^{m-1} B_l^{(p-1)}(\mathbf{q}_1, \dots, \mathbf{q}_l) B_{m-l}^{(1)}(\mathbf{q}_{l+1}, \dots, \mathbf{q}_m), & p > 1, \\ \frac{\mu_{1\dots m}}{q_{1\dots m}} G_m(\mathbf{q}_1, \dots, \mathbf{q}_m), & p = 1. \end{cases} \quad (\text{A.3})$$

Finally, to obtain a kernel Z_n that is symmetric in its arguments, we need A_n and $B_n^{(p)}$ symmetric and the sum over m in Eq. (A.1) must be symmetrized with respect to all permutations exchanging momenta from the $\{\mathbf{q}_1, \dots, \mathbf{q}_m\}$ set with the $\{\mathbf{q}_{m+1}, \dots, \mathbf{q}_n\}$ set. A_n is trivially symmetric provided that the standard F_n and G_n kernels are; we can make $B_n^{(p)}$ symmetric by symmetrizing the sum over l in Eq. (A.3) the same way.

We use Eq. (A.1) to implement an algorithm that evaluates the redshift-space kernels for a given set of momenta. Using the algorithm of Ref. [32] we can efficiently obtain F_n and G_n and thus A_n . We implement $B_n^{(p)}$ recursively utilizing memorization: we store results on a grid defined by n , p as well as an integer representing the momentum argument configuration, with a hash-function for easy lookup. Storing intermediate results greatly speeds up the algorithm due to the fact that the same combinations of n , p and argument configurations of $B_n^{(p)}$ appears several times in the recursive sum of Eq. (A.3), the double sum of Eq. (A.1) and additionally because of overlap between the different kernels required to compute loop corrections to the power spectrum (cf. Eq. (2.7)). Both authors independently implemented the algorithm in separate codes and checked that the calculated one- and two-loop corrections agree within Monte Carlo numerical uncertainty between the codes.

B Additional checks and supplementary results

In this appendix we perform various tests to validate our EFT framework at NNLO, and provide supplementary results. We check that the low- k limit of the numerical evaluation at two-loop has the appropriate scaling as required by mass and momentum conservation in Sec. B.1. Next, in Sec. B.2 we confirm numerically that the EFT prescription has removed the cutoff-dependence of the bare theory by comparing EFT predictions with different cutoffs. We apply our method in real space in Sec. B.3. In Sec. B.4 we show the χ^2 corresponding to the fits shown in Sec. 3. In Sec. B.5 we add a proxy k^4 counterterm to the $NNLO$ results, and finally in Sec. B.6 we show results for the hexadecapole in redshift space.

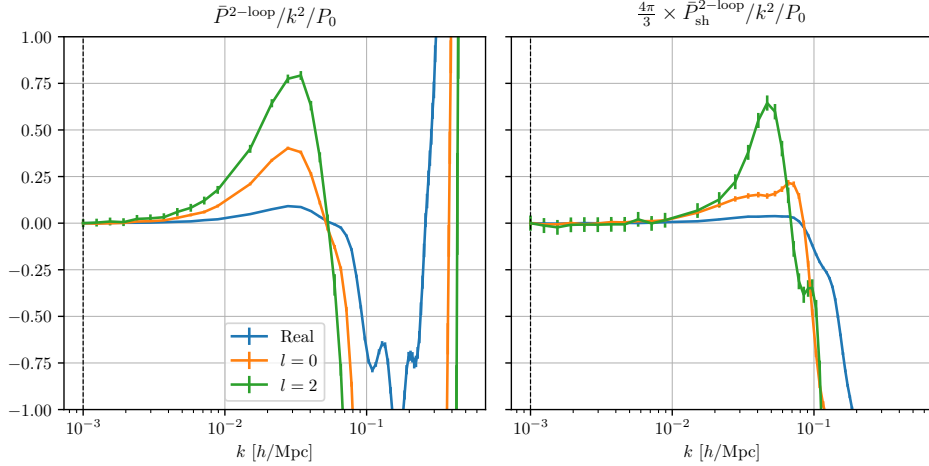


Figure 6. Subtracted two-loop (*left*) and single-hard two-loop (*right*) corrections. The graphs are normalized by $k^2 P_0(k)$ in order to highlight the double-hard scaling at low- k . For the real result, the spectrum P_0 used in the normalization stands for the IR-resummed input spectrum $P_{\text{nw}} + e^{-k^2 \Sigma^2} P_{\text{w}}$ in real space, and for the monopole and quadrupole it stands for the Kaiser spectrum computed with IR-resummed input spectrum $P_{\text{nw}} + e^{-k^2 \Sigma_{\text{tot}}^2} P_{\text{w}}$ in redshift space, projected onto the zeroth and second Legendre polynomials, respectively. The dashed line indicates the grid point at which the double-hard limit is fitted and removed. Errorbars correspond to numerical uncertainty from Monte Carlo integration.

B.1 Subtraction of double-hard contribution

As discussed in Sec. 2, we choose a renormalization scheme where we remove the double-hard contribution of the two-loop correction, so that the γ_1 parameter is a priori expected to retain the same value at NLO and NNLO. The double-hard limit is given analytically in App. C.3, however in practice we opt to measure this limit by considering the low- k limit of the two-loop correction. At $k \sim 10^{-3} h \text{ Mpc}^{-1}$ the two-loop integral has only support for $q_1, q_2 \gg k$ (the linear power spectrum is suppressed on large scales), corresponding to the double-hard limit. Thus, we may fit and remove the double-hard $k^2 P_0(k)$ contribution. This is shown in the left panel of Fig. 6. We display the *subtracted* two-loop correction, i.e. after the double-hard contribution has been removed. The graphs are normalized to $k^2 P_0(k)$, which means that the subtraction amounts to shifting them by a constant so that the low- k limit goes to zero. We see indeed that for $k \lesssim 0.004 h \text{ Mpc}^{-1}$ the real result, the monopole and the quadrupole all approach a plateau around zero, confirming that the numerical result exhibits the correct double-hard limit, which can be renormalized by the γ_1 counterterm.

Similarly, the right panel of Fig. 6 displays the subtracted single-hard limits of the two-loop corrections, normalized to $k^2 P_0(k)$. Again, we observe a plateau at low- k , affirming the appropriate scaling of the “hard limit of the single-hard limit” in the numerical result. Compared to the full two-loop (right panel), the single-hard reaches the $k^2 P_0(k)$ scaling for even larger k , $k \lesssim 0.01 h \text{ Mpc}^{-1}$, because q_1 is hard (in the numerics $q_1 = 10 h \text{ Mpc}^{-1}$). We check that the k -scaling of the numerical single-hard result matches the analytic results provided in App. C.1.

B.2 Cutoff-dependence

In this section we demonstrate that the renormalization in the EFT setup we adopt indeed leads to a cutoff-independent prediction for the power spectrum in redshift space, by computing results for two additional values of the cutoff to the fiducial results shown in Sec. 3. The comparison is displayed in Fig. 7. In the upper panels we plot the monopole (left) and quadrupole (right) power spectrum divided by the Quijote result for three different cutoffs: $\Lambda_- = 0.7 h \text{ Mpc}^{-1}$, $\Lambda = 1 h \text{ Mpc}^{-1}$ (fiducial value used in main text) and $\Lambda_+ = 1.3 h \text{ Mpc}^{-1}$. The lower panels show the residuals between Λ_+/Λ_- and Λ . We see that the different cutoffs yield results that completely agree within numerical

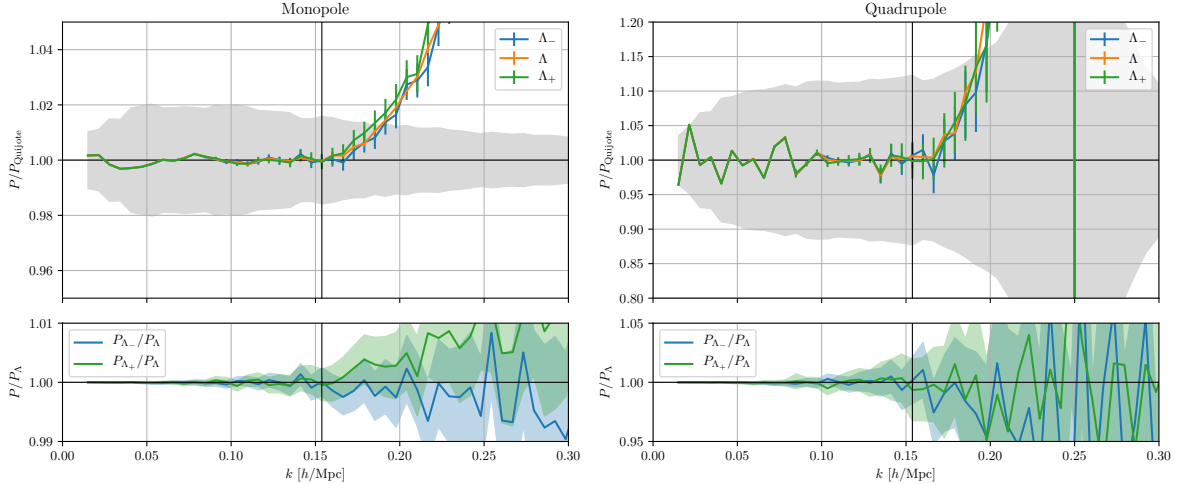


Figure 7. Monopole and quadrupole contributions for different values of the cutoff: $\Lambda_- = 0.7h \text{ Mpc}^{-1}$, $\Lambda = 1h \text{ Mpc}^{-1}$ (our fiducial value) and $\Lambda_+ = 1.3h \text{ Mpc}^{-1}$. *Upper panel:* predictions are normalized to Quijote, with the gray shaded region indicating simulation uncertainty. *Lower panel:* fractional difference between the results using cutoffs Λ_- and Λ_+ versus Λ .

uncertainty from the Monte Carlo integration, demonstrating that the counterterms in Eq. (2.17) appropriately correct for the cutoff-dependence of the bare theory. The comparison is shown for a pivot scale $k_{\text{max}} = 0.15h \text{ Mpc}^{-1}$, however we find the same conclusion for the other pivot scales used in this work.

B.3 Real space

Next, we validate our method in real space. We use Eq. (2.9) and the IR-resummation of Eq. (2.16), where in real space $\Sigma_{\text{tot}}^2 = \Sigma^2$. In Fig. 8 we show fits of perturbative results in real space to Quijote N -body data for different pivot scales. The calibration cases are the same as those presented in Sec. 3: we show 0/1-parameters NLO as well as the 2-parameter NNLO results. As was the case in redshift space, if we use pivot scales of $k_{\text{max}} = 0.15h \text{ Mpc}^{-1}$ or $0.2h \text{ Mpc}^{-1}$, the standard 1-parameter NLO model features spurious k -dependence that we interpret as overfitting. Hence, we include also a 0-parameter NLO fit, using γ_1 as measured from the NNLO fit, which should reduce the amount of overfitting and thus provide a more faithful estimate for the wavenumber reach of the NLO prediction. Using again $k_{\text{max}} = 0.15h \text{ Mpc}^{-1}$ as our fiducial pivot scale, we find that adding the two-loop correction extends the wavenumber reach that matches Quijote data within sampling uncertainty from $k = 0.13h \text{ Mpc}^{-1}$ to $k = 0.2h \text{ Mpc}^{-1}$. As expected, due to the smaller relative importance of higher-order corrections in real space than in redshift space, perturbation theory in real space matches N -body results down to somewhat smaller scales than in redshift space, although the difference is not very large at $z = 0$.

In total, we find that we can accurately match the Quijote N -body simulation result to $k \simeq 0.2h \text{ Mpc}^{-1}$ at $z = 0$ with perturbation theory at NNLO, using two EFT parameters, consistent with previous studies at two-loop [30, 36].

B.4 Chi-squared

The χ^2 per d.o.f. (Eq. 3.1) at $z = 0$ is shown in Fig. 9 for the monopole/quadrupole and for the different calibration cases discussed in Sec. 3. The small $\chi^2/\text{d.o.f.} \ll 1$ suggests that our estimator for the N -body error is too simple, e.g. not accounting for covariance of different bins, however we are here only interested in the relative performance of each case, not the overall χ^2 value. As concluded in Sec. 3, the 0-parameter NLO fit (green) matches the Quijote data up to $k = 0.1h \text{ Mpc}^{-1}$, and indeed beyond this wavenumber we observe a steep increase in $\chi^2/\text{d.o.f.}$ Although relatively smaller than the 0-parameter result, the $\chi^2/\text{d.o.f.}$ of the 1-parameter NLO case (orange) also increases beyond

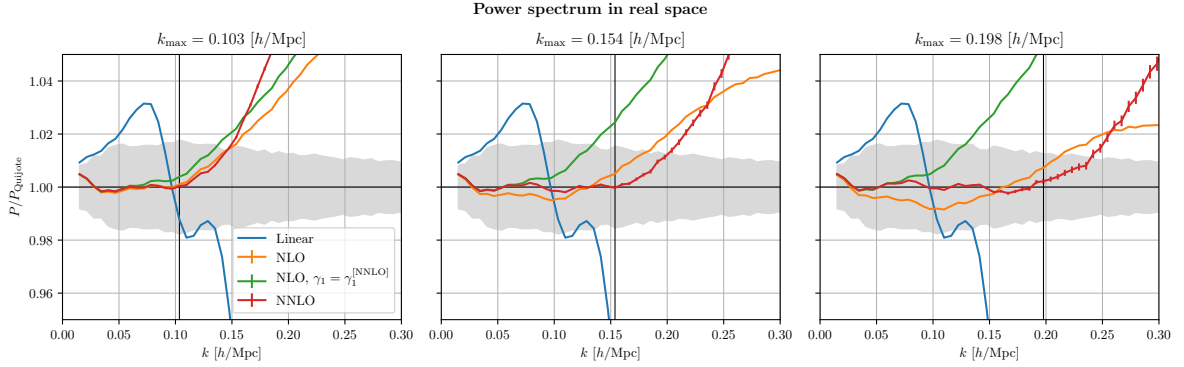


Figure 8. Perturbative predictions for the power spectrum in real space at redshift $z = 0$. The linear (blue), 0- (green) and 1-parameter (orange) NLO as well as NNLO (red) approximations are shown. The results are normalized to Quijote N -body data, and its uncertainty is displayed in gray.

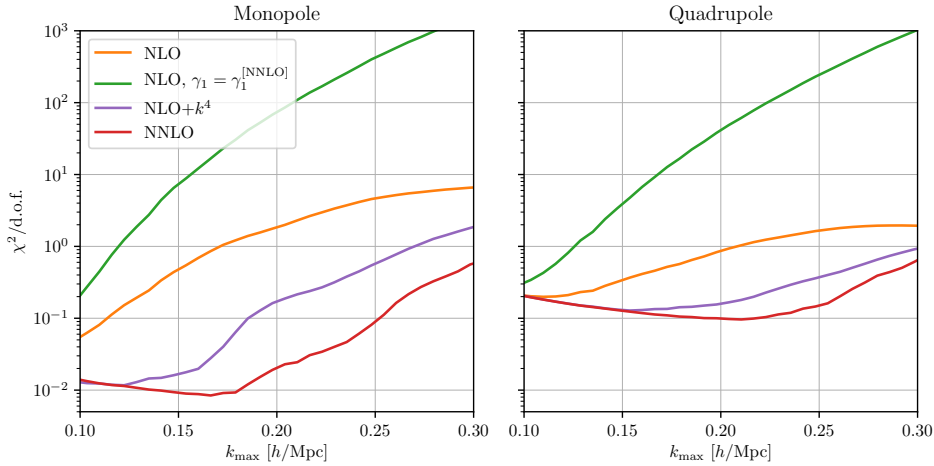


Figure 9. Reduced χ^2 for the various perturbative orders and calibration schemes (see Sec. 3), plotted as a function of the pivot scale k_{\max} .

$k = 0.1h \text{ Mpc}^{-1}$, indicating a worsening of the fit from this point. Adding a proxy k^4 counterterm to the NLO (purple), extends the range of scales with good agreement for this NLO 2-parameter model to $k \simeq 0.15h \text{ Mpc}^{-1}$. Nevertheless, it is clear that the full NNLO 2-parameter model (red) is required to accurately match Quijote data up to $k \simeq 0.18h \text{ Mpc}^{-1}$. We note that when lowering k_{\max} below $0.1h \text{ Mpc}^{-1}$, the fit becomes increasingly affected by sample variance of the Quijote data, i.e. the available simulation data become insufficient to reliably determine the EFT parameters in that case. We therefore do not display lower k_{\max} values in Fig. 9.

B.5 Add k^4 counterterm to NNLO prediction

We investigate whether adding a $k^4 P_l^{\text{lin}}(k)$ counterterm to the NNLO result yields any improvement. This 3-parameter NNLO model is plotted in Fig. 10 (purple line), normalized to Quijote simulation data at $z = 0$. We find that adding the $k^4 P_l^{\text{lin}}(k)$ term does not improve the fit compared to the 2-parameter NNLO case. Note that the leading contribution at small k of the subtracted single-hard two-loop correction is in fact proportional to $k^4 P_l^{\text{lin}}(k)$ (the double-hard limit $\propto k^2 P_l^{\text{lin}}(k)$ is subtracted off). While this may be viewed to provide an explanation for the observed degeneracy of the single-hard and k^4 counterterms, we note that the single-hard counterterm deviates from $k^4 P_l^{\text{lin}}(k)$ scaling

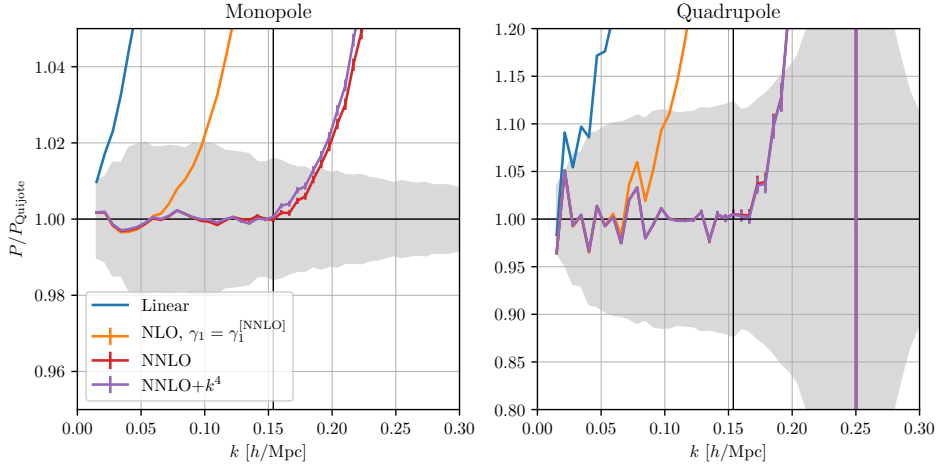


Figure 10. Impact of introducing a proxy $k^4 P_l^{\text{lin}}(k)$ counterterm at NNLO. The purple line shows the outcome of adding this counterterm, corresponding to a 3-parameter fit at NNLO. The 0-parameter NLO (orange) and 2-parameter NNLO (red) are shown for comparison (with purple being almost on top of red lines, especially for the quadrupole). A pivot scale $k_{\text{max}} = 0.15h \text{ Mpc}^{-1}$ is used. All graphs are normalized to Quijote data, whose uncertainty is indicated by gray shading.

already at $k \simeq 0.05h \text{ Mpc}^{-1}$. Nevertheless, within the region where it yields a sizable contribution we find that the k -dependence of the single-hard correction is at least approximately close to a $k^4 P_l^{\text{lin}}(k)$ shape. We also checked that adding the k^4 counterterm has no significant impact when increasing the pivot scale to $k_{\text{max}} = 0.2h \text{ Mpc}^{-1}$.

B.6 Hexadecapole

Finally, in this section we apply our analysis to the hexadecapole in redshift space. The results are displayed in Fig. 11. Due to the limited number of modes in the simulations on large scales, and their distribution in μ -space, the simulation estimate poorly recovers the hexadecapole for $k \lesssim 0.1h \text{ Mpc}^{-1}$. Nevertheless, the EFT coefficients at NNLO can be reasonably calibrated for $0.1h \text{ Mpc}^{-1} < k < 0.15h \text{ Mpc}^{-1}$. At NLO, it is more challenging to reliably measure γ_1 , therefore we show the NLO result using γ_1 measured at NNLO. We can estimate that the NLO result is in agreement with the simulations (within sample variance uncertainty) up to $k \approx 0.14h \text{ Mpc}^{-1}$ and the NNLO up to $k \approx 0.22h \text{ Mpc}^{-1}$.

C Analytical results for the single- and double-hard limits

In this appendix we derive an analytical result for the single-hard EFT correction $\bar{P}_{l,\text{sh}}^{2\text{-loop}}(k; \Lambda)$ defined in Eq. (2.12) that renormalizes contributions to the two-loop power spectrum in redshift space for which one of the loop wavenumbers is large, see Sec. C.1. In Sec. C.2 we provide some intermediate results related to the single-hard limit for reference.

In addition, we provide an expression for the difference between the bare two-loop contribution $P_l^{2\text{-loop}}(k; \Lambda)$ and the quantity $\bar{P}_l^{2\text{-loop}}(k; \Lambda)$ used in our analysis, related to the double-hard limit, see Sec. C.3.

C.1 Single-hard EFT counterterm

The integrand for the two-loop power spectrum in redshift space is given in Eq. (2.7). In the single-hard limit $q_1 \rightarrow \infty$,

$$\begin{aligned}
 p_{s,L=2}(\mathbf{k}, \mu, \mathbf{q}_1, \mathbf{q}_2) \rightarrow \frac{1}{q_1^2} \left[(30Z_5^\infty(\mathbf{k}, \mathbf{q}_2, -\mathbf{q}_2)Z_1(\mathbf{k}) + 9Z_3^\infty(\mathbf{k})Z_3(\mathbf{k}, \mathbf{q}_2, -\mathbf{q}_2)) P_0(k) \right. \\
 \left. + 12Z_4^\infty(\mathbf{k} - \mathbf{q}_2, \mathbf{q}_2)Z_2(\mathbf{k} - \mathbf{q}_2, \mathbf{q}_2)P_0(|\mathbf{k} - \mathbf{q}_2|) \right] + \mathcal{O}(1/q_1^4), \quad (\text{C.1})
 \end{aligned}$$

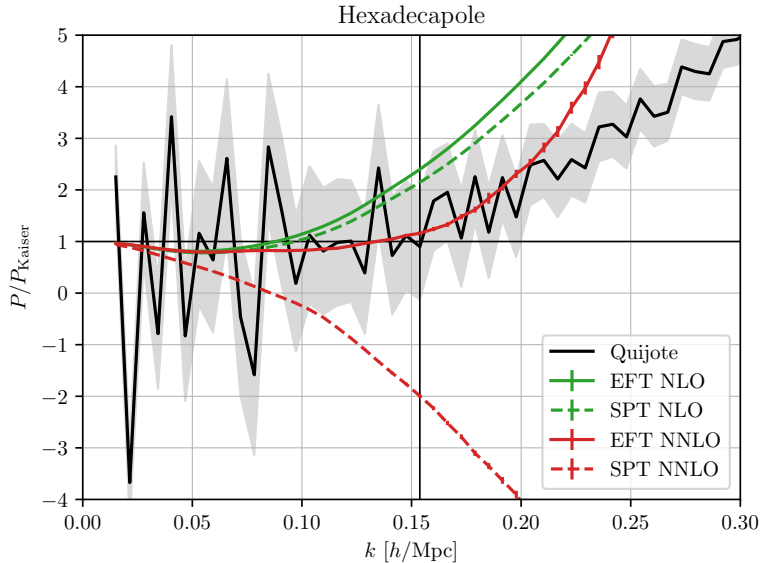


Figure 11. Perturbation theory predictions and Quijote simulation result for the power spectrum hexadecapole, normalized to the linear Kaiser prediction. Sample variance uncertainty from the N -body simulations is indicated with gray bands. The green solid lines correspond to a 0-parameter NLO prediction (as described in Sec. 3) and the red lines show our 2-parameter NNLO results. SPT results are displayed with dashed lines.

where we defined the asymptotic UV limit

$$Z_n^\infty(\mathbf{k}_1, \dots, \mathbf{k}_{n-2}) \equiv \int \frac{d\Omega_p}{4\pi} p^2 Z_n(\mathbf{k}_1, \dots, \mathbf{k}_{n-2}, \mathbf{p}, -\mathbf{p})|_{p \rightarrow \infty}, \quad (\text{C.2})$$

which exists due to the scaling of the kernels $Z_n \propto p^{-2} + \mathcal{O}(p^{-4})$ imposed by mass and momentum conservation. For $n = 3$,

$$Z_3^\infty(\mathbf{k}) = -\frac{k^2}{1890} (61 + 183f\mu_k^2 + 3f^2\mu_k^2(83 + 46\mu_k^2) + 105f^3\mu_k^4), \quad (\text{C.3})$$

where $\mu_k = (\mathbf{k} \cdot \hat{z})/k$. Results for $n = 4, 5$ are given below. Apart from mass/momentum conservation constraints, we checked that our implementation of the Z_n kernels satisfy Eq. (2.5).

Using the definition of the single-hard EFT correction Eq. (2.12), we find

$$P_{l,\text{sh}}^{2\text{-loop}}(k; \Lambda) = 2 \times 3 \times (A_l(k; \Lambda) + B_l(k; \Lambda)), \quad (\text{C.4})$$

with

$$\begin{aligned} A_l(k; \Lambda) &\equiv \frac{2l+1}{2} \int_{-1}^1 d\mu_k \mathcal{P}_l(\mu_k) \int_{\mathbf{q}_2}^\Lambda P_0(q_2) (30Z_5^\infty(\mathbf{k}, \mathbf{q}_2, -\mathbf{q}_2)Z_1(\mathbf{k}) + 9Z_3^\infty(\mathbf{k})Z_3(\mathbf{k}, \mathbf{q}_2, -\mathbf{q}_2)) P_0(k), \\ B_l(k; \Lambda) &\equiv \frac{2l+1}{2} \int_{-1}^1 d\mu_k \mathcal{P}_l(\mu_k) \int_{\mathbf{q}_2}^\Lambda P_0(q_2) 12Z_4^\infty(\mathbf{k} - \mathbf{q}_2, \mathbf{q}_2)Z_2(\mathbf{k} - \mathbf{q}_2, \mathbf{q}_2)P_0(|\mathbf{k} - \mathbf{q}_2|). \end{aligned} \quad (\text{C.5})$$

Following [30] we subtract the contribution to the single-hard limit that is already accounted for by the leading $k^2 P_0(k)$ EFT correction (see also Sec. C.3). This amounts to using $\bar{P}_{l,\text{sh}}^{2\text{-loop}}(k; \Lambda) = 2 \times 3 \times (\bar{A}_l(k; \Lambda) + B_l(k; \Lambda))$ where $\bar{A}_l(k; \Lambda)$ differs from $A_l(k; \Lambda)$ by the replacement of Z_5^∞ by

$$\bar{Z}_5^\infty(\mathbf{k}, \mathbf{q}_2, -\mathbf{q}_2) \equiv Z_5^\infty(\mathbf{k}, \mathbf{q}_2, -\mathbf{q}_2) - Z_5^\infty(\mathbf{k}, \mathbf{q}_2, -\mathbf{q}_2)|_{q_2 \rightarrow \infty}. \quad (\text{C.6})$$

In order to perform the integration over μ_k we write $\mu_k = \hat{z} \cdot \mathbf{k}/k$, where \hat{z} is a generic unit vector in the direction of the line-of-sight (not necessarily related to the third coordinate direction). Similarly,

$\mu_{q_2} = \hat{z} \cdot \mathbf{q}_2/q_2$. Due to rotational invariance of the (multipole-projected) power spectrum we can trade the integration over μ_k by an angular average over \hat{z} , $\frac{1}{2} \int d\mu_k \mapsto \int \frac{d\Omega_{\hat{z}}}{4\pi}$. This allows us to interchange the integration over \mathbf{q}_2 with the average over the \hat{z} direction. After performing the latter, the integrand only depends on the magnitudes k and q_2 as well as $c = \mathbf{k} \cdot \mathbf{q}_2/(kq_2)$. The integration over c can then also be performed for \bar{A}_l . Using the results from Sec. C.2 we find

$$\begin{aligned}\bar{A}_l(k; \Lambda) &= 4\pi k^4 P_0(k) \int_0^\Lambda dq_2 P_0(q_2) \bar{a}_l(k/q_2), \\ B_l(k; \Lambda) &= 2 \times 4\pi k^4 \int_0^\Lambda dq_2 \frac{1}{2} \int_{-1}^{\min(1, k/(2q_2))} dc P_0(q_2) P_0(\sqrt{k^2 + q_2^2 - 2kq_2c}) b_l(k/q_2, c),\end{aligned}\quad (\text{C.7})$$

where we used the symmetry under $\mathbf{q}_2 \rightarrow \mathbf{k} - \mathbf{q}_2$ to limit the integration domain to $|\mathbf{k} - \mathbf{q}_2| > q_2$ for B_l , leading to the additional factor of two and the upper limit for c . We find

$$\begin{aligned}\bar{a}_l(x) &= \frac{1}{444972528000x^6} f_l(x) + \frac{(x^2 - 1)^3}{118659340800x^7} \log\left(\frac{x+1}{x-1}\right)^2 g_l(x), \\ b_l(x, c) &= -\frac{1}{12978365400(1 - 2cx + x^2)^2} h_l(c, x),\end{aligned}\quad (\text{C.8})$$

where

$$\begin{aligned}f_0(x) &= -122574375 + 1934903250x^2 - 4063378900x^4 + 6891099950x^6 - 494386725x^8 \\ &+ f(-245148750 + 3869806500x^2 - 8126757800x^4 + 13782199900x^6 - 988773450x^8) \\ &+ f^2(-202153875 + 7398335770x^2 - 16721366060x^4 + 29724212070x^6 - 2014729185x^8) \\ &+ f^3(-35238060 + 8064808440x^2 - 18792501312x^4 + 37724885640x^6 - 2540596500x^8) \\ &+ f^4(36636600 + 3304341040x^2 - 6875228360x^4 + 30783953200x^6 - 2116274160x^8) \\ &+ f^5(378378000x^2 - 504504000x^4 + 11471860400x^6 - 504504000x^8) + 1373372000f^6x^6, \\ g_0(x) &= -8171625 + 107202550x^2 + 32959115x^4 + f(-16343250 + 214405100x^2 + 65918230x^4) \\ &+ f^2(-13476925 + 457283918x^2 + 134315279x^4) + f^3(-2349204 + 531389352x^2 + 169373100x^4) \\ &+ f^4(2442440 + 226802576x^2 + 141084944x^4) + f^5(25225200x^2 + 33633600x^4), \\ h_0(x, c) &= 13 \times [21635040c^2 - 50500800c^4 - 15798720cx + 57731520c^3x + 50500800c^5x - 58822470c^2x^2 \\ &- 17613960c^4x^2 + 29417640cx^3 - 46938570c^3x^3 + 24166065c^2x^4 + 315(-6176 + 25933x^2) \\ &+ f(43270080c^2 - 101001600c^4 - 31597440cx + 115463040c^3x + 101001600c^5x - 117644940c^2x^2 \\ &- 35227920c^4x^2 + 58835280cx^3 - 93877140c^3x^3 + 48332130c^2x^4 + 630(-6176 + 25933x^2)) \\ &+ f^2(-44344832c^2 - 93438912c^4 - 7964992cx + 275567488c^3x + 93438912c^5x - 373557016c^2x^2 \\ &+ 70702856c^4x^2 + 156483950cx^3 - 239765624c^3x^3 + 100203334c^2x^4 \\ &+ 7(2490944 + 6232451x^2 + 230153x^4)) \\ &+ f^3(-88197888c^2 - 36840960c^4 + 17642496cx + 250077696c^3x + 36840960c^5x - 403308012c^2x^2 \\ &+ 179937000c^4x^2 + 172087356cx^3 - 321486564c^3x^3 + 122697960c^2x^4 \\ &+ 12(1959872 + 3689138x^2 + 230153x^4)) \\ &+ f^4(-23255232c^2 - 3360896c^4 + 36915648cx + 53232256c^3x + 3360896c^5x - 129287774c^2x^2 \\ &+ 121484440c^4x^2 + 64401260cx^3 - 205997330c^3x^3 + 81545849c^2x^4 \\ &+ 77(-59136 + 8797x^2 + 62818x^4)) \\ &+ f^5(5103840c^2x^2 + 26493320c^4x^2 - 1502340cx^3 - 58090480c^3x^3 + 27018110c^2x^4 \\ &+ 51450x^2(-35 + 54x^2)) \\ &+ f^6(2160900c^2x^2 + 1440600c^4x^2 - 2521050cx^3 - 5042100c^3x^3 + 3361400c^2x^4 \\ &+ 60025x^2(3 + 7x^2))],\end{aligned}\quad (\text{C.9})$$

$$\begin{aligned}
f_2(x) &= 10 \times [f(-49029750 + 773961300x^2 - 1625351560x^4 + 2756439980x^6 - 197754690x^8) \\
&\quad + f^2(-66284625 + 1936481900x^2 - 4323380890x^4 + 7488463140x^6 - 515039685x^8) \\
&\quad + f^3(-6344910 + 2439070140x^2 - 5703792432x^4 + 11373993540x^6 - 769234050x^8) \\
&\quad + f^4(17069325 + 1142872640x^2 - 2450137690x^4 + 9972981200x^6 - 681352035x^8) \\
&\quad + f^5(146191500x^2 - 214987500x^4 + 3959655700x^6 - 174856500x^8) \\
&\quad + 499408000f^6x^6], \\
g_2(x) &= 10 \times [f(-3268650 + 42881020x^2 + 13183646x^4) + f^2(-4418975 + 117314860x^2 + 34335979x^4) \\
&\quad + f^3(-422994 + 161476692x^2 + 51282270x^4) + f^4(1137955 + 79226056x^2 + 45423469x^4) \\
&\quad + f^5(9746100x^2 + 11657100x^4)], \\
h_2(x, c) &= 5 \times [f(225004416c^2 - 525208320c^4 - 164306688cx + 600407808c^3x + 525208320c^5x \\
&\quad - 611753688c^2x^2 - 183185184c^4x^2 + 305943456cx^3 - 488161128c^3x^3 + 251327076c^2x^4 \\
&\quad + 3276(-6176 + 25933x^2)) \\
&\quad + f^2(-4713488c^2 - 873754752c^4 - 205533952cx + 1756936480c^3x + 873754752c^5x \\
&\quad - 2246440066c^2x^2 + 215752394c^4x^2 + 996332246cx^3 - 1554059234c^3x^3 + 680064385c^2x^4 \\
&\quad + 13(5390960 + 22198982x^2 + 230153x^4)) \\
&\quad + f^3(-504592608c^2 - 481241280c^4 + 15377856cx + 1971667776c^3x + 481241280c^5x \\
&\quad - 3104672272c^2x^2 + 1273977640c^4x^2 + 1371167616cx^3 - 2555882784c^3x^3 + 991770780c^2x^4 \\
&\quad + 52(3135992 + 7041278x^2 + 230153x^4)) \\
&\quad + f^4(-196948752c^2 - 67523456c^4 + 248696448cx + 528944416c^3x + 67523456c^5x \\
&\quad - 1267193564c^2x^2 + 1145203150c^4x^2 + 661661000cx^3 - 1918651280c^3x^3 + 745214834c^2x^4 \\
&\quad + 182(-94776 + 253747x^2 + 132643x^4)) \\
&\quad + f^5(-15887760c^2x^2 + 311402840c^4x^2 + 38073000cx^3 - 606917920c^3x^3 + 267402800c^2x^4 \\
&\quad + 20580x^2(-539 + 827x^2)) \\
&\quad + f^6(16206750c^2x^2 + 20888700c^4x^2 - 17647350cx^3 - 57984150c^3x^3 + 34874525c^2x^4 \\
&\quad + 60025x^2(12 + 49x^2))]. \tag{C.10}
\end{aligned}$$

Note that all a_l and b_l approach a finite limit for both $x \rightarrow 0$ (i.e. $q_2 \gg k$) and $x \rightarrow \infty$ (i.e. $q_2 \ll k$). In the latter limit, we checked that the constant terms cancel in the sum $a_l(x) + \int_{-1}^1 dc b_l(x, c) \propto 1/x$, as required by Galilean invariance, and similarly to the usual analogous cancellation at one-loop order.

For the various angular averages we used

$$\int \frac{d\Omega_q}{4\pi} (\hat{v}_1 \cdot \hat{q})^{n_1} \cdots (\hat{v}_N \cdot \hat{q})^{n_N} = \left(\frac{\partial}{\partial \lambda_1} \right)^{n_1} \cdots \left(\frac{\partial}{\partial \lambda_N} \right)^{n_N} \frac{\sinh |\sum_i \lambda_i \hat{v}_i|}{|\sum_i \lambda_i \hat{v}_i|} \Big|_{\lambda_i=0}, \tag{C.11}$$

which can be readily shown by computing $\int \frac{d\Omega_q}{4\pi} e^{\sum_i \lambda_i \hat{v}_i \cdot \hat{q}}$. Here $\hat{q} = \mathbf{q}/|\mathbf{q}|$.

C.2 Single-hard limit of Z_4 and Z_5

$$\begin{aligned}
Z_4^\infty(\mathbf{k} - \mathbf{q}, \mathbf{q}) = & -\frac{k^2}{4074840(1 - 2cx + x^2)} \left[-6176 + 48096c^2 - 48096c^3x + 25933x^2 - 16892c^2x^2 \right. \\
& + cx(-35744 + 32879x^2) \\
& + f\mu_k(11\mu_q(16032c - 8016x - 16032c^2x + 2038cx^2 + 2989x^3) + \mu_k(-16032c^3x \\
& + c^2(16032 - 89986x^2) + 4(-6176 + 25933x^2) + cx(-54800 + 98637x^2))) \\
& + 33f^2\mu_k^2(4752 + 7443x^2 + 4190\mu_k^2x^2 - 2c^2(3379 + 539\mu_k^2)x^2 + \mu_q^2(5456 - 5456cx + 2377x^2) \\
& + \mu_k\mu_qx(-5456 - 5276cx + 2989x^2) + cx(-9504 + 49(83 + 46\mu_k^2)x^2)) \\
& + 1617f^3\mu_k^3x^2(46\mu_k^2\mu_qx + 83\mu_q(-2c + x) + \mu_k(78 - 30c^2 - 46\mu_q^2 + 35cx)) \\
& \left. + 56595f^4\mu_k^4\mu_qx^2(-\mu_q + \mu_kx) \right], \tag{C.12}
\end{aligned}$$

$$\begin{aligned}
Z_5^\infty(\mathbf{k}, \mathbf{q}, -\mathbf{q}) = & -\frac{k^2}{264864600(1 - 2cx + x^2)(1 + 2cx + x^2)} \left[1832216c^2 - 173536c^4 + 1763891c^2x^2 \right. \\
& - 6602262c^4x^2 + 382844c^6x^2 + 861688c^2x^4 + 1462930c^4x^4 \\
& - 427427c^2x^6 + 4(1 + x^2)(32614 + 79843x^2) \\
& + f\mu_k(26c\mu_q(299792 + 496133x^2 + 69608c^4x^2 + 223706x^4 - 32879x^6 \\
& + 4c^2(-7888 - 283775x^2 + 27573x^4)) + \mu_k(104412c^6x^2 + 20(32614 \\
& + 112457x^2 + 79843x^4) + c^4(-47328 - 3498710x^2 + 4447058x^4) \\
& - c^2(-1366488 + 4080003x^2 + 1507916x^4 + 1282281x^6))) \\
& + 13f^2\mu_k^2(-197960c^3\mu_k\mu_qx^2 + 774232c^3\mu_k\mu_qx^4 - 2c\mu_k\mu_q(-76192 + 152041x^2 \\
& + 113650x^4 + 98637x^6) + 4c^4x^2(-10811 + 45866\mu_q^2 + 127953x^2 + 98\mu_k^2(43 + 568x^2)) \\
& - c^2(-62072 + (2392381 + 1073122\mu_k^2)x^2 + 4(67831 + 53144\mu_k^2)x^4 + 1617(83 + 46\mu_k^2)x^6 \\
& + \mu_q^2(75016 + 2733892x^2 - 84136x^4)) - (-1 - x^2)(521816 + 611822x^2 \\
& + 4\mu_k^2(52700 + 87371x^2) - 7\mu_q^2(-97432 - 88787x^2 + 4697x^4))) \\
& + 429f^3\mu_k^3(56c^3\mu_q(249 + 61\mu_q^2)x^2 + 392c^3(83 + 35\mu_k^2)\mu_qx^4 + 980c^4\mu_kx^2(1 + 5x^2) \\
& - c^2\mu_kx^2(28185 + 7952x^2 + 1715x^4 - 4\mu_q^2(-5344 + 3101x^2)) - 14c\mu_qx^2(244\mu_q^2 \\
& + 83(19 + 14x^2 + 7x^4) + 14\mu_k^2(23 + 24x^2 + 23x^4)) + \mu_k(-1 - x^2)(-2(2376 + 5617x^2) \\
& + \mu_q^2(-5456 - 2019x^2 + 2989x^4))) \\
& + 21021f^4\mu_k^4\mu_qx^2(160c^3\mu_kx^2 + 4c^2\mu_q(15 + (98 + 46\mu_k^2)x^2) - 10c\mu_k(7 + 2x^2 + 7x^4) \\
& - \mu_q(1 + x^2)(143 + 83x^2 + 46\mu_k^2(1 + x^2))) \\
& \left. - 735735f^5\mu_k^6\mu_q^2x^2(1 + (2 - 4c^2)x^2 + x^4) \right]. \tag{C.13}
\end{aligned}$$

We used the abbreviations $x = k/q$ and $c = \mathbf{k} \cdot \mathbf{q}/(kq)$. We checked that our results for Z_n^∞ for $n = 3, 4, 5$ agree with those for the corresponding density kernels F_n^∞ (see e.g. [30, 50]) in the formal limit when setting the growth rate f to zero. We also used Eq. (2.5) for further cross-checks in the limit $q \ll k$ ($x \rightarrow \infty$).

C.3 Double-hard limit

Contributions to the two-loop power spectrum for which both wavenumbers are large, $q_1, q_2 \gg k$, are degenerate with the EFT counterterm γ_1 proportional to $k^2 P_0(k)$ that was already introduced to renormalize the one-loop result. We therefore choose the option to subtract these contributions in our analysis. Note that this is not strictly necessary, and would merely lead to different values of γ_1 . The subtracted two-loop contribution is given by

$$\bar{P}_l^{2\text{-loop}}(k; \Lambda) \equiv P_l^{2\text{-loop}}(k; \Lambda) - P_{l,\text{dh}}^{2\text{-loop}}(k; \Lambda). \tag{C.14}$$

The double-hard limit is given by

$$P_{l,\text{dh}}^{2\text{-loop}}(k; \Lambda) = \frac{2l+1}{2} \int_{-1}^1 d\mu_k \mathcal{P}_l(\mu_k) \int_{\mathbf{q}_1}^{\Lambda} \int_{\mathbf{q}_2}^{\Lambda} P_0(q_1) P_0(q_2) 30 Z_5(\mathbf{k}, \mathbf{q}_1, -\mathbf{q}_1, \mathbf{q}_2, -\mathbf{q}_2) |_{q_i \rightarrow \infty} Z_1(\mathbf{k}) P_0(k), \quad (\text{C.15})$$

where the Z_5 kernel is evaluated in the limit where both loop wavenumbers becomes large, with fixed ratio q_1/q_2 . It can be written as

$$P_{l,\text{dh}}^{2\text{-loop}}(k; \Lambda) = 30k^2 P_0(k) \int_{\mathbf{q}_1}^{\Lambda} \int_{\mathbf{q}_2}^{\Lambda} P_0(q_1) P_0(q_2) \frac{1}{q_1 q_2} Z_{l,\text{dh}}^{15}(q_1/q_2). \quad (\text{C.16})$$

Using techniques similar as above we find

$$Z_{l,\text{dh}}^{15}(x) = \frac{1+x^2}{238378140000x^5} p_l(x) + \frac{(x^2-1)^4}{63567504000x^6} \log\left(\frac{x+1}{x-1}\right)^2 q_l(x), \quad (\text{C.17})$$

where here $x = q_1/q_2$ with

$$\begin{aligned} p_0(x) &= 1155(5760 + 13605x^2 - 128258x^4 + 13605x^6 + 5760x^8) \\ &\quad + 2310f(5760 + 13605x^2 - 128258x^4 + 13605x^6 + 5760x^8) \\ &\quad + 7f^2(1193760 + 31353255x^2 - 159738358x^4 + 31353255x^6 + 1193760x^8) \\ &\quad + 234f^3(6240 + 660295x^2 - 3151542x^4 + 660295x^6 + 6240x^8) \\ &\quad + 7078500f^4x^2(3 - 14x^2 + 3x^4), \\ q_0(x) &= -1155(384 + 2699x^2 + 384x^4) - 2310f(384 + 2699x^2 + 384x^4) \\ &\quad - 7f^2(79584 + 2461609x^2 + 79584x^4) - 234f^3(416 + 45961x^2 + 416x^4) - 1415700f^4x^2, \\ p_2(x) &= 10[462f(5760 + 13605x^2 - 128258x^4 + 13605x^6 + 5760x^8) \\ &\quad + 11f^2(233640 + 4284945x^2 - 22623562x^4 + 4284945x^6 + 233640x^8) \\ &\quad + 13f^3(42120 + 3453585x^2 - 16590346x^4 + 3453585x^6 + 42120x^8) \\ &\quad + 2359500f^4x^2(3 - 14x^2 + 3x^4)], \\ q_2(x) &= -10[462f(384 + 2699x^2 + 384x^4) + 11f^2(15576 + 358351x^2 + 15576x^4) \\ &\quad + 13f^3(2808 + 243343x^2 + 2808x^4) + 471900f^4x^2]. \end{aligned} \quad (\text{C.18})$$

Note that $Z_{l,\text{dh}}^{15}(x) = Z_{l,\text{dh}}^{15}(1/x)$. For $f = 0$ this result agrees with the double-hard limit of the real space power spectrum (see e.g. [30, 50]). Furthermore, we checked a correspondence of the double-hard limit and the ‘‘hard limit of the single-hard limit’’. More precisely, we checked that for the single-hard contribution, the difference between $P_{l,\text{sh}}^{2\text{-loop}}(k; \Lambda)$ and $\bar{P}_{l,\text{sh}}^{2\text{-loop}}(k; \Lambda)$ (see subtraction term in Eq. (C.6)) can be related to Eq. (C.16) evaluated with $Z_{l,\text{dh}}^{15}(x)|_{x \rightarrow \infty}$. Note that the leading term in $Z_{l,\text{dh}}^{15}(x)$ is scaling as $\propto 1/x$ for large x , such that the integrand in Eq. (C.16) scales as $1/(q_1 q_2 x) = 1/q_1^2$.

References

- [1] N. Kaiser, *Clustering in real space and in redshift space*, *Mon. Not. Roy. Astron. Soc.* **227** (1987) 1.
- [2] BOSS collaboration, *The clustering of galaxies in the completed SDSS-III Baryon Oscillation Spectroscopic Survey: cosmological analysis of the DR12 galaxy sample*, *Mon. Not. Roy. Astron. Soc.* **470** (2017) 2617 [1607.03155].
- [3] DESI collaboration, *The DESI Experiment Part I: Science, Targeting, and Survey Design*, **1611.00036**.
- [4] L. Amendola et al., *Cosmology and fundamental physics with the Euclid satellite*, *Living Rev. Rel.* **21** (2018) 2 [1606.00180].
- [5] F. Bernardeau, S. Colombi, E. Gaztanaga and R. Scoccimarro, *Large scale structure of the universe and cosmological perturbation theory*, *Phys. Rept.* **367** (2002) 1 [astro-ph/0112551].

- [6] S. Pueblas and R. Scoccimarro, *Generation of Vorticity and Velocity Dispersion by Orbit Crossing*, *Phys. Rev. D* **80** (2009) 043504 [0809.4606].
- [7] D. Baumann, A. Nicolis, L. Senatore and M. Zaldarriaga, *Cosmological Non-Linearities as an Effective Fluid*, *JCAP* **07** (2012) 051 [1004.2488].
- [8] H. Gil-Marín et al., *The clustering of galaxies in the SDSS-III Baryon Oscillation Spectroscopic Survey: RSD measurement from the LOS-dependent power spectrum of DR12 BOSS galaxies*, *Mon. Not. Roy. Astron. Soc.* **460** (2016) 4188 [1509.06386].
- [9] BOSS collaboration, *The clustering of galaxies in the completed SDSS-III Baryon Oscillation Spectroscopic Survey: Anisotropic galaxy clustering in Fourier-space*, *Mon. Not. Roy. Astron. Soc.* **466** (2017) 2242 [1607.03150].
- [10] BOSS collaboration, *The clustering of galaxies in the completed SDSS-III Baryon Oscillation Spectroscopic Survey: Cosmological implications of the Fourier space wedges of the final sample*, *Mon. Not. Roy. Astron. Soc.* **467** (2017) 2085 [1607.03143].
- [11] BOSS collaboration, *The clustering of galaxies in the completed SDSS-III Baryon Oscillation Spectroscopic Survey: On the measurement of growth rate using galaxy correlation functions*, *Mon. Not. Roy. Astron. Soc.* **469** (2017) 1369 [1607.03148].
- [12] BOSS collaboration, *The clustering of galaxies in the completed SDSS-III Baryon Oscillation Spectroscopic Survey: cosmological implications of the configuration-space clustering wedges*, *Mon. Not. Roy. Astron. Soc.* **464** (2017) 1640 [1607.03147].
- [13] T. Tröster et al., *Cosmology from large-scale structure: Constraining Λ CDM with BOSS*, *Astron. Astrophys.* **633** (2020) L10 [1909.11006].
- [14] A. Semenaite et al., *Cosmological implications of the full shape of anisotropic clustering measurements in BOSS and eBOSS*, *Mon. Not. Roy. Astron. Soc.* **512** (2022) 5657 [2111.03156].
- [15] M. M. Ivanov, M. Simonović and M. Zaldarriaga, *Cosmological Parameters from the BOSS Galaxy Power Spectrum*, *JCAP* **05** (2020) 042 [1909.05277].
- [16] G. D’Amico, J. Gleyzes, N. Kokron, K. Markovic, L. Senatore, P. Zhang et al., *The Cosmological Analysis of the SDSS/BOSS data from the Effective Field Theory of Large-Scale Structure*, *JCAP* **05** (2020) 005 [1909.05271].
- [17] S.-F. Chen, Z. Vlah and M. White, *A new analysis of galaxy 2-point functions in the BOSS survey, including full-shape information and post-reconstruction BAO*, *JCAP* **02** (2022) 008 [2110.05530].
- [18] M. Garny, D. Laxhuber and R. Scoccimarro, *Perturbation theory with dispersion and higher cumulants: Framework and linear theory*, *Phys. Rev. D* **107** (2023) 063539 [2210.08088].
- [19] M. Garny, D. Laxhuber and R. Scoccimarro, *Perturbation theory with dispersion and higher cumulants: Nonlinear regime*, *Phys. Rev. D* **107** (2023) 063540 [2210.08089].
- [20] J. C. Jackson, *Fingers of God: A critique of Rees’ theory of primordial gravitational radiation*, *Mon. Not. Roy. Astron. Soc.* **156** (1972) 1P [0810.3908].
- [21] R. Scoccimarro, H. M. P. Couchman and J. A. Frieman, *The Bispectrum as a Signature of Gravitational Instability in Redshift-Space*, *Astrophys. J.* **517** (1999) 531 [astro-ph/9808305].
- [22] R. Scoccimarro, *Redshift-space distortions, pairwise velocities and nonlinearities*, *Phys. Rev. D* **70** (2004) 083007 [astro-ph/0407214].
- [23] A. Eggemeier, B. Camacho-Quevedo, A. Pezzotta, M. Crocce, R. Scoccimarro and A. G. Sánchez, *COMET: Clustering observables modelled by emulated perturbation theory*, *Mon. Not. Roy. Astron. Soc.* **519** (2022) 2962 [2208.01070].
- [24] V. Desjacques, D. Jeong and F. Schmidt, *The Galaxy Power Spectrum and Bispectrum in Redshift Space*, *JCAP* **12** (2018) 035 [1806.04015].
- [25] L. Senatore and M. Zaldarriaga, *Redshift Space Distortions in the Effective Field Theory of Large Scale Structures*, **1409.1225**.
- [26] S.-F. Chen, Z. Vlah and M. White, *Consistent Modeling of Velocity Statistics and Redshift-Space Distortions in One-Loop Perturbation Theory*, *JCAP* **07** (2020) 062 [2005.00523].

- [27] A. Taruya, T. Nishimichi and D. Jeong, *Grid-based calculations of redshift-space matter fluctuations from perturbation theory: UV sensitivity and convergence at the field level*, *Phys. Rev. D* **105** (2022) 103507 [2109.06734].
- [28] A. Taruya, T. Nishimichi and F. Bernardeau, *Precision modeling of redshift-space distortions from a multipoint propagator expansion*, *Phys. Rev. D* **87** (2013) 083509 [1301.3624].
- [29] A. Taruya, T. Nishimichi and S. Saito, *Baryon Acoustic Oscillations in 2D: Modeling Redshift-space Power Spectrum from Perturbation Theory*, *Phys. Rev. D* **82** (2010) 063522 [1006.0699].
- [30] T. Baldauf, L. Mercolli and M. Zaldarriaga, *Effective field theory of large scale structure at two loops: The apparent scale dependence of the speed of sound*, *Phys. Rev. D* **92** (2015) 123007 [1507.02256].
- [31] D. Blas, M. Garny and T. Konstandin, *On the non-linear scale of cosmological perturbation theory*, *JCAP* **09** (2013) 024 [1304.1546].
- [32] D. Blas, M. Garny and T. Konstandin, *Cosmological perturbation theory at three-loop order*, *JCAP* **01** (2014) 010 [1309.3308].
- [33] M. M. Ivanov and S. Sibiryakov, *Infrared Resummation for Biased Tracers in Redshift Space*, *JCAP* **07** (2018) 053 [1804.05080].
- [34] M. Crocce and R. Scoccimarro, *Renormalized cosmological perturbation theory*, *Phys. Rev. D* **73** (2006) 063519 [astro-ph/0509418].
- [35] J. J. M. Carrasco, M. P. Hertzberg and L. Senatore, *The Effective Field Theory of Cosmological Large Scale Structures*, *JHEP* **09** (2012) 082 [1206.2926].
- [36] M. Garny and P. Taule, *Two-loop power spectrum with full time- and scale-dependence and EFT corrections: impact of massive neutrinos and going beyond EdS*, *JCAP* **09** (2022) 054 [2205.11533].
- [37] A. Chudaykin, M. M. Ivanov, O. H. E. Philcox and M. Simonović, *Nonlinear perturbation theory extension of the Boltzmann code CLASS*, *Phys. Rev. D* **102** (2020) 063533 [2004.10607].
- [38] D. J. Eisenstein, H.-j. Seo and M. J. White, *On the Robustness of the Acoustic Scale in the Low-Redshift Clustering of Matter*, *Astrophys. J.* **664** (2007) 660 [astro-ph/0604361].
- [39] M. Crocce and R. Scoccimarro, *Nonlinear Evolution of Baryon Acoustic Oscillations*, *Phys. Rev. D* **77** (2008) 023533 [0704.2783].
- [40] L. Senatore and M. Zaldarriaga, *The IR-resummed Effective Field Theory of Large Scale Structures*, *JCAP* **02** (2015) 013 [1404.5954].
- [41] T. Baldauf, M. Mirbabayi, M. Simonović and M. Zaldarriaga, *Equivalence Principle and the Baryon Acoustic Peak*, *Phys. Rev. D* **92** (2015) 043514 [1504.04366].
- [42] Z. Vlah, U. Seljak, M. Y. Chu and Y. Feng, *Perturbation theory, effective field theory, and oscillations in the power spectrum*, *JCAP* **03** (2016) 057 [1509.02120].
- [43] D. Blas, M. Garny, M. M. Ivanov and S. Sibiryakov, *Time-Sliced Perturbation Theory II: Baryon Acoustic Oscillations and Infrared Resummation*, *JCAP* **07** (2016) 028 [1605.02149].
- [44] J. Hamann, S. Hannestad, J. Lesgourgues, C. Rampf and Y. Y. Y. Wong, *Cosmological parameters from large scale structure - geometric versus shape information*, *JCAP* **07** (2010) 022 [1003.3999].
- [45] F. Villaescusa-Navarro et al., *The Quijote simulations*, *Astrophys. J. Suppl.* **250** (2020) 2 [1909.05273].
- [46] M. Garny and P. Taule, *Loop corrections to the power spectrum for massive neutrino cosmologies with full time- and scale-dependence*, *JCAP* **01** (2021) 020 [2008.00013].
- [47] M. Lewandowski, L. Senatore, F. Prada, C. Zhao and C.-H. Chuang, *EFT of large scale structures in redshift space*, *Phys. Rev. D* **97** (2018) 063526 [1512.06831].
- [48] T. Nishimichi, G. D’Amico, M. M. Ivanov, L. Senatore, M. Simonović, M. Takada et al., *Blinded challenge for precision cosmology with large-scale structure: results from effective field theory for the redshift-space galaxy power spectrum*, *Phys. Rev. D* **102** (2020) 123541 [2003.08277].
- [49] G. D’Amico, L. Senatore, P. Zhang and T. Nishimichi, *Taming redshift-space distortion effects in the EFTofLSS and its application to data*, [2110.00016](https://arxiv.org/abs/2110.00016).

- [50] T. Baldauf, M. Garny, P. Taule and T. Steele, *Two-loop bispectrum of large-scale structure*, *Phys. Rev. D* **104** (2021) 123551 [[2110.13930](#)].